Spatial patterns of aboveground phytogenic Si stocks in a grass-dominated catchment – Results from UAS based high resolution remote sensing

Marc Wehrhan[1], Daniel Puppe[2], Danuta Kaczorek[1,3], Michael Sommer[1,2,4]

[1] Leibniz Centre for Agricultural Landscape Research (ZALF), "Landscape Pedology" Working Group, 15374 Müncheberg, Germany
[2] Leibniz Centre for Agricultural Landscape Research (ZALF), "Silicon Biogeochemistry" Working Group, 15374 Müncheberg, Germany
[3] Warsaw University of Life Sciences (SGGW), Department of Soil Environment Sciences, 02-776 Warsaw, Poland
[4] University of Potsdam, Institute of Geography and Environmental Science, 14476 Potsdam, Germany

Correspondence to: Marc Wehrhan (wehrhan@zalf.de)

Abstract. Various studies have been performed to quantify silicon (Si) stocks in plant biomass and related Si fluxes in terrestrial biogeosystems. Most studies are deliberately designed on the plot scale to ensure low heterogeneity in soils and plant composition, hence similar environmental conditions. Due to the immanent spatial soil variability, the transferability of results to larger areas, such as catchments, is therefore limited. However, the emergence of new technical features and increasing knowledge on details in Si cycling leads to a more complex picture at landscape or catchment scales. Dynamic and static soil properties change along the soil continuum and might influence not only the species composition of natural vegetation, but its biomass distribution and related Si stocks. Maximum Likelihood (ML) classification was applied to multispectral imagery captured by an Unmanned Aerial System (UAS) aiming the identification of land cover classes (LCC). Subsequently, the Normalized Difference Vegetation Index (NDVI) and ground-based measurements of biomass were used to quantify aboveground Si stocks in two Si accumulating plants (*Calamagrostis epigejos* and *Phragmites australis*) in a heterogeneous catchment and related corresponding spatial patterns of these stocks to soil properties. We found aboveground Si stocks of *C. epigejos* and *P. australis* to be surprisingly high (maxima of Si stocks reach values up to 98 g Si m^{-2}), i.e., comparable to or markedly exceeding reported values for the Si storage in aboveground vegetation of various terrestrial ecosystems. We further found spatial patterns of plant aboveground Si stocks to reflect spatial heterogeneities in soil properties. From our results, we concluded that (i) aboveground biomass of plants seems to be the main factor of corresponding phytogenic Si stock quantities and (ii) a detection of biomass heterogeneities via UAS-based remote sensing represents a promising tool for the quantification of lifelike phytogenic Si pools at landscape scales.

1 Introduction

Biogenic silicon (BSi), i.e., silica precipitates ($SiO_2 \cdot n H_2O$) synthesized by various organisms, has been recognized as a key factor controlling Si fluxes from terrestrial to aquatic ecosystems (Dürr et al., 2011; Street-Perrott and Barker, 2008; Struyf

and Conley, 2012), which mainly results from its pool size and a larger solubility compared to silicate minerals (e.g., Cornelis and Delvaux, 2016). Eukaryotic and prokaryotic organisms, i.a., plants, bacteria, fungi, diatoms, testate amoebae, and sponges, are able to synthesize BSi (Clarke, 2003; Ehrlich et al., 2010), and corresponding BSi pools can be found in terrestrial biogeosystems (Puppe et al., 2015; Puppe, 2020; Sommer et al., 2006). BSi structures of different origin indicate differences in their physicochemical surface properties (Puppe and Leue, 2018), which in turn control their dissolution kinetics (Bartoli, 1985; Fraysse et al., 2006, 2009). In most terrestrial ecosystems phytogenic Si, i.e., BSi synthesized by plants, generally represents the largest BSi pool in soil-plant systems, hence exerts the strongest influence on Si fluxes into soils (reviewed by Schaller et al., 2021). In agricultural soil-plant systems the recycling of phytogenic Si has been found to boost the biological Si feedback loop and to compensate for Si losses by crop harvest (Alexandre et al., 1997; Blecker et al., 2006; Cornelis et al., 2010; Yang et al., 2020; Li et al., 2020; Puppe et al., 2021).

For the majority of higher plants Si is considered as a beneficial element, because various positive effects of Si accumulation in plants have been revealed, i.e., increased plant growth and resistance against abiotic and biotic stresses (e.g., Epstein, 2009; Ma and Yamaji, 2006; Puppe and Sommer, 2018). In this context, especially grasses of the family Poaceae (or Gramineae) are known as strong Si accumulators (Hodson et al., 2005; Katz et al., 2021), and corresponding Si storage in aboveground vegetation, e.g., in the Great Plains or the tropical humid grass savanna, has been found to be an important driver in Si cycling (Blecker et al., 2006; Alexandre et al., 2011). Various studies have been performed to quantify Si stocks and fluxes in/from the above- and belowground plant biomass (e.g., Alexandre et al., 1997; Bartoli, 1983; Cornelis et al., 2010; Sommer et al., 2013; Turpault et al., 2018). Most of these studies were performed at (sequences of) small-scale plots ($<10^2$ m^2) with intended low heterogeneity in soils and plant canopy composition. Often results were extrapolated to larger spatial units up to global scale implicitly assuming similar environmental conditions (e.g., Carey and Fulweiler, 2012). However, the emergence of new technical features and increasing knowledge on details in Si cycling (e.g., the role of lateral fluxes) leads to a more complex picture at landscape or catchment scales. Dynamic and static soil properties change along the soil continuum and might influence not only the species composition of natural vegetation, but its biomass distribution and related Si stocks. In fact, changes in soil properties have been found to affect Si bioavailability in soils leading to changes in plant Si concentrations (e.g., Li et al., 2019) with consequences for plant performance and ecosystem functioning (reviewed by Katz et al., 2021).

Remote sensing represents an efficient tool to provide spatially consistent information on environmental objects, conditions and properties. To identify different land covers or to assess biodiversity indicators, supervised classification techniques such as Maximum Likelihood (ML) has found wide acceptance (Fuller et al., 1998; Otukei et al., 2010; Shafri et al., 2007; Strecha et al., 2012; Gonzáles et al., 2015). A widespread method for the derivation of quantitative canopy properties is the use of vegetation indices (VIs) in combination with ground-based measurements (Thenkabail et al., 2002; Lelong et al., 2008; Zarco-Tajeda et al., 2012). VIs are linear, orthogonal or ratio combinations of reflectance calculated from different wavelengths ranging from the visible (VIS) to the near-infrared (NIR) part of the electromagnetic spectrum (Bouman, 1992) and found to be appropriate proxies for temporal and spatial variation in vegetation canopies and biophysical parameters (Gao et al., 2000; Haboudane et al., 2004). In particular, the Normalized Difference Vegetation Index (NDVI), as the most commonly used VI,

relates reflectance in red (sensitive to chlorophyll absorption) and near-infrared (sensitive to canopy and leaf structure) wavebands (Rouse, 1974). Numerous satellite based studies applied VIs to quantify biophysical vegetation parameters either of crops (Moran et al., 1995; Kross et al., 2015), grassland (Gammon et al., 1995; Wang et al., 2005), pristine or near-natural

70 ecosystems (Kim et al., 2015; Cui et al., 2018). The recent development of Unmanned Aerial Systems (UAS) offers new options for high-resolution observations at landscape and catchment scale.

Numerous missions have been conducted over hardly accessible areas or protected ecosystems such as wetlands (Strecha et al., 2012; Zweig et al., 2015), riparian zones of lakes and rivers (Husson et al., 2014; Husson et al., 2016), estuarine tidal flats (Kaneko and Nohara, 2014), riparian forests (Dunford et al., 2009) and Antarctic moss beds (Turner et al, 2014). Most of the

75 studies delineated the patchy and small-scale distribution of plant communities and identified individual species by using of-the-shelf (partly modified) compact digital cameras providing an adequate sub-decimeter resolution in VIS and NIR spectral wavelengths. Successful preprocessing workflows were developed for UAS imagery as a prerequisite for accurate image interpretation (Laliberte et al., 2011; Berni et al., 2009; Kelcey and Lucieer, 2012; Lelong et al., 2008; Wehrhan et al., 2016). However, none of these studies addressed both the classification of species composition and the quantification of respective

80 aboveground biomass fractions. To the best of our knowledge there is no study published until now, which finally quantifies aboveground plant Si accumulation and its spatial distribution using UAS remote sensing in a heterogeneous catchment and relates the spatial patterns to relevant soil properties.

In the current study, we apply UAS-based remote sensing to the grass-dominated, artificially catchment "Chicken Creek". It represents an ideal study site for Si cycling at catchment scale for several reasons. Firstly, the vegetation dynamics as well as

85 soil development have been intensively monitored ab initio (e.g., Elmer et al., 2013; Zaplata et al., 2011a, b). From this data base the site-specific appearance and spread of two predominant Si accumulators, *Calamagrostis epigejos* and *Phragmites australis* (both belonging to the Poaceae family), can be derived, which allows an estimation of mean annual Si uptake rates. Secondly, extensive soil data (repetitive sampling campaigns) are available at a 20 m x 20 m grid (Gerwin et al. 2011). Potentially important drivers for the observed spatial patterns of plants, such as the soil texture and nutrients can be withdrawn

90 from these data. Thirdly, previous studies already clarified the BSi pool dynamics in soils at Chicken Creek during initial pedogenesis (Puppe et al., 2014, 2016, 2017, 2018). Here, we present a methodological approach to quantify the Si stocks of two Si accumulators (i.e., *C. epigejos* and *P. australis*) at catchment scale and their relationship to soil-related drivers. In detail we want to answer three major research questions:

(i) How large are aboveground phytogenic Si stocks?

95 (ii) To which extent are spatial patterns of *C. epigejos* and *P. australis* and corresponding Si stocks driven by initial soil properties?

(iii) What are the benefits and limitations of UAS-based remote sensing of phytogenic Si stocks?

2 Methods

2.1 Study Area

100   The artificial catchment "Chicken Creek" (6 ha in size, thereof 5.3 ha fenced) was constructed in an open-cast mining area of Lusatia, Germany (51.6049° N, 14.2667° E) in 2004–2005 (construction finished in September 2005). A 2-4 m thick, surficial layer of Quaternary, sandy sediment was dumped on a 1–2 m pan-shaped layer of Tertiary clays, which seals the whole catchment at its base. In the lower part of the catchment, additional clay dams were constructed on top of the clay layer (transverse to the slope). These dams act as a stabilization barrier preventing the sandy substrate from sliding downhill and

105   serve as a funnel to direct groundwater flow into the artificial pond downstream (Gerwin et al., 2010). Due to the artificial construction, the lower boundary conditions of the catchment site are clearly defined including knowledge about the 3D sediment structures (Gerke et al. 2013, Schneider et al., 2011). The construction work left a bare land surface on which natural vegetation could develop without disturbance (natural succession) but also created a zonal pattern of soil properties caused by the natural heterogeneity of the parent material taken from different areas in the fore-field according to the progression of the

110   mine (Gerwin et al., 2009) (Fig. 1).
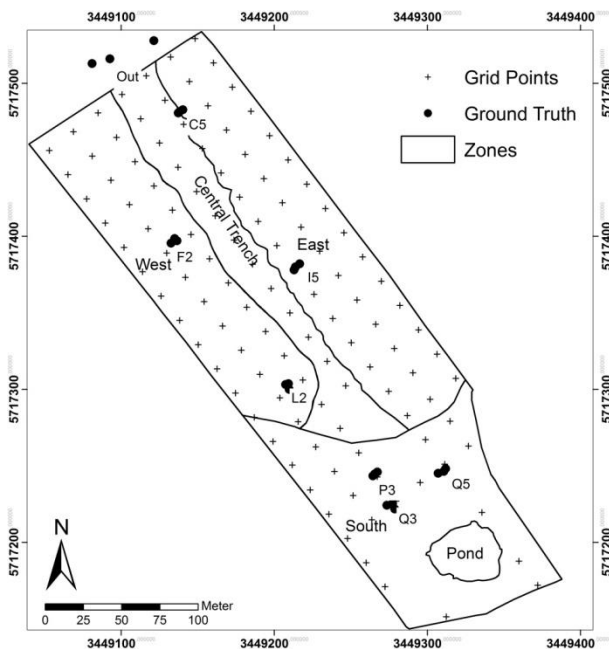
Figure 1: Schematic map of the artificial catchment "Chicken Creek" showing grid points, ground truth sites and zones, delineating
115   **areas with slightly different soil properties.**

C. epigejos has been present since the very beginning and belonged to the most dominating species since 2010, especially in the western part of the catchment. *P. australis* has also been present from the beginning of vegetation development in 2006,

but it was mainly restricted to the area around the pond in the southern part of the catchment (Elmer et al., 2011, Schaaf et al., 2010). The sub-continental climate is characterized by a mean annual precipitation of 563 mm and a mean annual temperature of 8.9 °C.

2.2 Ground-based measurements

2.2.1 Aboveground biomass

Ground-based measurements were carried out on 22 August 2014, one day after the UAS mission. Shoot biomass (include stems, leaves and inflorescence) with a dominance of *C. epigejos* was sampled at sites C5, F2, I5 and L2, which represent raster points equipped for an extensive soil moisture and temperature monitoring. Three additional sites (CA1 to CA3) were sampled outside of the fenced area to include sites of high population densities (Fig. 1). At each site plants were cut within an area of 50 cm x 50 cm (0.25 m²) from three locations, which represent a (local) gradient of low, medium and high population densities. Analogous, three sites close to raster points P3, Q2 and Q5 with a dominant occurrence of *P. australis* were sampled. The dead, tufted biomass of *C. epigejos* and the brown shoots including the litter of *P. australis* were sampled separately within the same areas. This material of the preceding seasons is referred to as litter hereafter. A subset of the brown *P. australis* shoots have been retained for further analysis in order to find out whether the Si content is different from green shoots or not. All plant samples were oven-dried at 105 °C for 48 h to further determine the Si content.

2.2.2. Si analysis of plant material

An aliquot of 5 g from the dried plant material was used to determine the Si content. The collected plant material was carefully washed with distilled water to remove adhering soil particles and oven-dried at 45°C. Subsequently the samples were milled using a knife mill (Grindomix GM 200, Retsch) in two steps: 4000 rpm for 1 min. and then 10000 rpm for 3 min. Sample aliquots of approximately 100 mg were digested under pressure in PFA digestion vessels using a mixture of 4 ml distilled water, 5 ml nitric acid (65%), and 1 ml hydrofluoric acid (40%) at 190 °C using a microwave digestion system (Mars 6, CEM). A second digestion step was used to neutralize the hydrofluoric acid with 10 ml of a 4%-boric acid solution at 150 °C. Silicon was measured by ICP-OES (ICP-iCAP 6300 Duo, Thermo Fisher Scientific GmbH) with an internal standard. To avoid contamination, only plastic equipment was used during the complete procedure. Analyses were performed in three lab replicates.

2.2.3. Soil sampling and soil analysis

Soil sampling of the upper 30 cm was carried out subsequent to catchment completion in 2005 at 124 grid points in a 20 m x 20 m grid (see Fig. 1). Soil samples were analysed on various physicochemical properties (for details see Gerwin et al., 2010). From these we used data of clay and nitrogen (N), which are known as important drivers for vegetation development at Chicken Creek (Elmer et al., 2013, Zaplata et al., 2011a, b). In addition, we analyzed the plant available potassium (K), phosphorus (P),

and Si content in retained samples from 2005 to evaluate their effects on spatial patterns of *C. epigejos* and *P. australis* and corresponding aboveground phytogenic Si stocks.

150   The plant available K and P were determined with the double-lactate method which is used in Germany for the determination of plant available potassium and phosphorus. The extraction solution comprises a 0.04 m calcium lactate solution buffered with 0.02 m hydrochloric acid at pH of 3.6 using a soil-to-solution ratio of 1:50 (VDLUFA, 1991). Four grams of air dried soil (<2 mm) were weighed into polyethylene laboratory bottles. Afterwards, 200 mL of extraction solution were added into those bottles and placed on a mechanical shaker for 90 min. After filtration, the phosphorus concentration was determined by

155   colorimetry (Gallery Plus, Microgenics) and the potassium concentration was measured using Flame-Atomic absorption spectroscopy (AAS-iCE 3300, Thermo Fischer). The reported values are in mg K or P per 100 g dry soil.

Plant available Si (water-extractable Si, cf. Sauer et al., 2006) was determined as described in Puppe et al. (2017). In short, ten grams of dry soil (<2 mm) was weighed, put into 80 mL centrifuge tubes, and 50 mL distilled water was added into it with three drops of a 0.1% NaN_3 solution to prevent microbial activity. Total extraction time was 7 days. Twice a day tubes were

160   gently shaken for 20 s by hand to prevent abrasion of mineral particles from colliding during constant (mechanical) shaking by using, e.g., a roll mixer. After extraction solutions were centrifuged (4000 rpm, 20 min), filtrated (0.45 µm polyamide membrane filters), and Si was measured via ICP–OES (ICP-iCAP 6300 DUO, Thermo Fisher Scientific Inc). Only plastic equipment was used during the complete extraction procedure to exclude any Si contamination. Analyses of water-extractable Si were performed at a minimum of two lab replicates per sample.

165   The alkaline extractant Tiron ($C_6H_4Na_2O_8S_2 \cdot H_2O$) was used for the detection of potential differences in the amorphous silica stocks (as a proxy of synthesized biogenic and pedogenic siliceous structures representing the main source for plant available Si), although a partial dissolution of primary minerals is well known (Sauer et al., 2006). However, due to the fact that the suitability of the so-called DeMaster technique (which represents the de facto standard method) for quantification of amorphous biogenic Si has been recently questioned (Meunier et al., 2014; Li et al., 2019), we performed no time-course

170   extraction using a short time extraction (1 h) for all samples. Based on the short extraction time of only one hour we excluded extensive extraction of mineral Si forms (cf. Kaczorek et al., 2019). The Tiron extractable Si (Si_{Tiron}) was determined according to the method developed by Biermans and Baert (1977), modified by Kodama and Ross (1991). The extraction solution was produced by dilution of 31.42 g Tiron with 800 mL of distilled water, followed by addition of 100 mL sodium carbonate solution (5.3 g Na_2CO_3 + 100 mL distilled water) under constant stirring. The final pH of 10.5 was reached by adding small

175   volumes of a 4M NaOH-solution. For the extraction 30 mg of dry soil were weighed into 80 mL centrifuge tubes and a 30 mL aliquot of the Tiron solution was added into it. The tubes were then heated at 80°C in a water bath for 1h. The extracted solutions were centrifuged at 4000 rpm for 30 min, filtrated (0.45 µm polyamide membrane filters, Whatman NL 17) and Si concentrations measured by ICP-OES. To avoid contamination, only plastic equipment was used during the complete procedure. Analyses of Tiron extractable Si was performed in three lab replicates per sample.

 2.3 UAS remote sensing

We used a fixed-wing UAS Carolo P360 (Fig. 2) with a wingspan of 3.6 m and a take-off weight of 22.5 kg. The UAS is equipped with a 12-band multi-camera array Mini-MCA 12 (MCA hereafter) (Tetracam Inc., CA, USA). The 12 narrow-band filters (between 10 nm and 40 nm bandwidth) cover the spectral range from visible to near infrared wavelengths with focus on the characteristic reflectance features of healthy vegetation (chlorophyll absorption band around 660 nm, the red-edge region

185   between 680 nm and 750 nm) and one of the water absorption bands around 950 nm. Hereafter, bands are denoted according their respective center wavelength in nm (e.g. b_{713} for the red edge band).

Figure 2: Unmanned Aerial System (UAS) Carolo P360 with multi-camera array Mini-MCA 12 (visible lenses at the underside of the camera).

190   The UAS mission was conducted during the flowering period of *C. epigejos* on 21 August 2014 under acceptable flight conditions (moderate wind speed and little cloud shadow). A small negligible area was covered in the south-east part with no or little occurrence of *C. epigejos* and *P. australis* respectively. At this time, the foliage is medium green and the large inflorescences are clearly visible. This facilitates the (i) spatial delineation and (ii) spectral distinction between *C. epigejos* populations and dozens of other existing grass-like species. Due to camera specifications a unique flight altitude of 163 m

195   above ground is required to achieve the desired ultrahigh ground sampling distance (GSD) of ~ 0.1 m. Details about UAS, camera specifications and mission settings are presented in appendix A1. The post-processing chain including radiometric corrections, mosaicking and geo-referencing is described in more detail in appendix A2.

2.4 Image classification

A supervised ML classification was applied to identify individual dominant plant species or communities. The ML classifier

200   requires a proper selected set of training areas for all objects visible in the image. For this purpose we used field inspections and available botanical mappings at grid points (data provided by M. Zaplata). Details regarding conditions and constraints of the ML classifier are given in appendix B1.

Finally 16 relevant land cover classes (LCC) were defined including three classes of non-vegetation (shadow, bare soil, open water) and four classes of legume and non-legume woods (Table 1). The statistical separability of the LCC signatures was

205 computed before each classification run. Divergence, an often used separability measure in remote sensing, is computed using the mean and variance-covariance matrices of the pixel values representing the training area. The Jeffries-Matusita (J-M) distance (Kavzoglu and Mather, 2000), the divergence measure used in this study, was computed for all possible LCC pairs. A computed value of zero indicates that classes are inseparable and a value of 1414 means total separability (Swain, 1978).

210 **Table 1: List of the 16 relevant land cover classes (LCC) as predefined for classification on basis of field survey and botanical mappings.**

Group	LCC No		Description
Grass-like communities	01	*C. epigejos* - d	Dense population
	02	*C. epigejos* - dt	Dense population close to trees (sunlit side of *Robinia pseudoacacia*)
	03	*C. epigejos* - m	Population with a minor fraction of visible Herbs, Mosses and Lichens
	04	*C. epigejos* - HML	Sparse population with a large fraction of visible Herbs, Mosses and lichens
	05	*P. australis* - d	Dense population with a particular fraction of shadow
	06	*P. australis* - m	Population with a minor fraction of other visible grass-like species and shadow
	07	*P. australis* – HML	Sparse population with a large fraction of visible Herbs, Mosses and lichens
	08	*F. rubra*	Population of *Festuca rubra agg.*
Legume-, non-legume Herbs; Mosses; Lichens (HML) communities	09	HML-0	Herbs, Mosses and lichens populations without any other visible grass-like species
	10	HML-1	Herbs, Mosses and lichens populations with a minor fraction of grass-like species (unidentified)
Legume-, non-legume Woods individuals	11	*R. pseudoacacia/S. caprea*	Large individuals of *Robinia pseudoacacia* and *Salix caprea*
	12	*H. rhamnoides*	Large individuals of *Hippophae rhamnoides*
	13	*P. sylvestris*	Small individuals of *Pinus sylvestris*
Non - vegetation	14	Shadow	Shadow of trees and bushes
	15	Bare soil	Predominately sandy substrate
	16	Open water	

2.5 Calculation of the Normalized Difference Vegetation Index (NDVI)

The NDVI is an intrinsic vegetation index that simply accounts for the chlorophyll absorption feature in the red (R) and the

215 structural information inherent in high NIR reflectance of a green vegetation canopy. It does not involve any external factor other than the measured spectral information and was calculated by:

$$NDVI = \frac{(NIR-R)}{(NIR+R)} \tag{1}$$

where NIR and R are the reflectance in the near-infrared and red band. Since radiometric calibration was renounced in this study, NIR and R refer to DNs instead of at-surface reflectance. In order to investigate the potential of the available bands in

220 the red edge (RE, the steep incline between VIS and NIR reflectance typically for green vegetation) and NIR domain, five

variations of the NDVI were calculated. The four NIR bands correspond to b_{831}, b_{861}, b_{899} and b_{953}. In case of the RE band b_{713}, NIR have to be substituted by RE in Eq. 1.

Coefficients of determination (R²s) were calculated for the relationships between the examined VIs and the ground measured fresh shoot biomass of *C. epigejos* and *P. australis* as individual species and for the pooled dataset consisting of all measures.

225 Since the fresh litter accumulated during the preceding seasons was covered by the tall growing *C. epigejos* and *P. australis* and therefore cannot be estimated directly, R²s were calculated analogous for the sum of the fresh shoot biomass and litter. The latter was done in order to find out whether correlations between calculated VIs and fresh shoot biomass at the one side, and -on the other hand-, between VIs and fresh shoot biomass including the litter can be used for an indirect estimation of fresh litter.

230 **2.6 Statistical analysis**

Correlations were analyzed using Spearman's rank correlation (r_s, monotonic relationships) and Pearson's correlation (r, linear relationships). Significances between independent samples were tested with the Kruskal-Wallis analysis of variance (ANOVA) followed by pairwise multiple comparisons (Dunn's post hoc test). Statistical analyses were performed using software package SPSS Statistics (version 22.0.0.0, IBM Corp.).

235 **3 Results**

3.1 Image classification

The computed J-M distance for the 120 LCC pairs showed an average of 1386 and a minimum of 1142. While the signatures of 79 LCCs were almost totaly separable (J-M distance ≥1 410), a fairly separability existed for 32 LCC pairs (J-M distance ≥ 1248). Values below 1249 were computed for 9 LCC pairs indicating a poor separability.

240 Figure 3 depicts the mean signatures of the 16 LCCs. In Fig. 3a all LCCs others than those classified as *C. epigejos* or *P. australis* (8 to 16) revealed large differences and could thus be clearly distinguished. While open water and shadow showed the lowest DNs over all spectral bands, the highest DNs in the visible range were characteristic for sandy soil (Stoner and Baumgarder, 1982). Regardless the use of DNs instead of reflectance the signatures of trees and bushes showed the characteristic features of green vegetation. With decreasing chlorophyll content and population densities of photosynthetically

245 active species (here *F. rubra*) and a simultaneously increasing fraction of shadow, cryptogam species and dead plant material (LCCs 9 and 10), DNs showed a more or less monotonous increase of DNs from the VIS to the NIR wavelength domain. The signatures of LCCs 1 to 7 are depicted in Fig. 3b.The signature of the dense *P. australis* population (LCC 5) exhibited a shape similar to the signatures of trees and bushes, but DNs were lower in the NIR domain influenced by a higher fraction of shadow visible to the sensor. All other signatures appeared similar regarding the general shape (monotonous increase), but the

250 separability was fairly high for most of them caused by the lower overall reflectance and the flatter slope of the signature with an increasing fraction of visible non-photosynthetic material and shadow. Amongst the 10 pairs showing poor separability, 4

pairs comprised LCCs describing transitional states within the same species (e.g. *P. australis*; LCC 6 and LCC 7) or couldn't clearly distinguish between *C. epigejos* and *P. australis*. The first case was uncritical as the respective LCCs were treated as one LCC in the further analysis. The second case couldn't be avoided due to co-occurrence within the same area of interest. However, resulting misclassifications were negligible with respect to the small differences of Si content observed for both species.
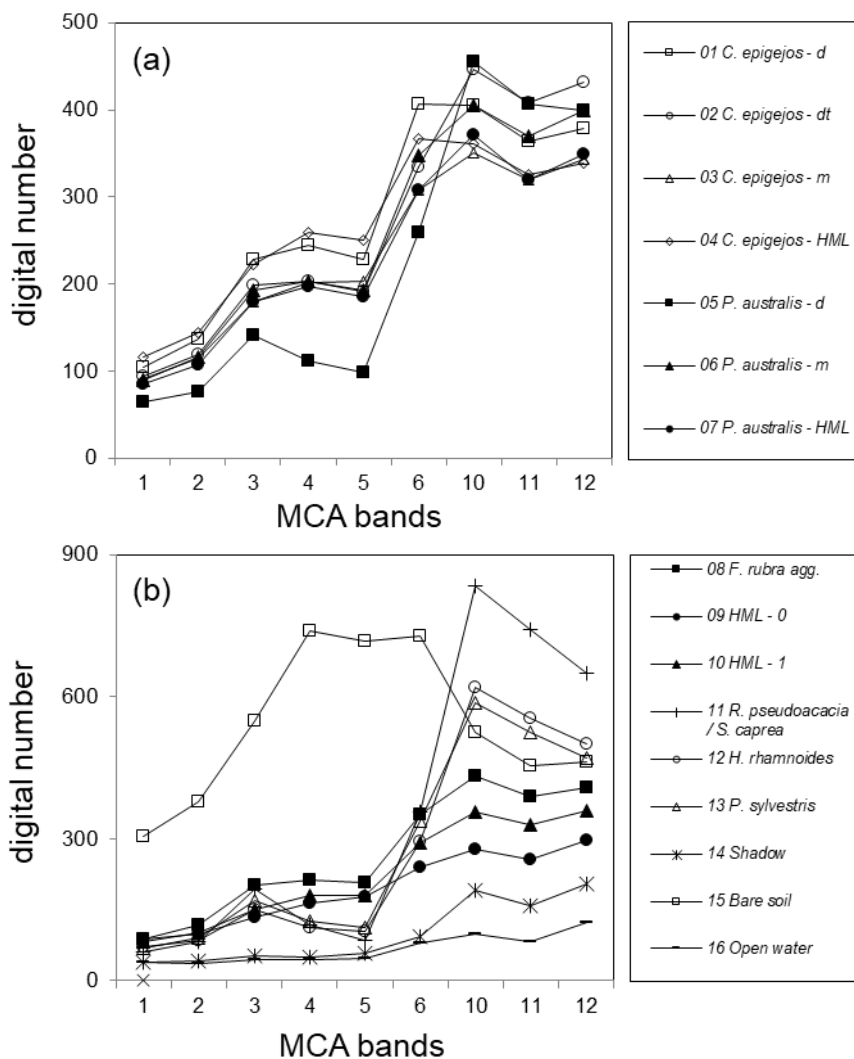
Figure 3: Mean signatures of classified LCCs others than *C. epigejos* and *P. australis* (a) and respective signatures of *C. epigejos* and *P. australis* classes (b). Note the different scaling of the y-axes.

Constraints had to be accepted regarding the poor separability between *F. rubra* (LCC 8), *C. epigejos* (LCC 2) and *P. australis* (LCC 6 and 7) respectively. Although mean signatures indicated fairly separabilty at least in the NIR domain, class variances were large and diminished the separability.

3.2 Spatial coverage and zonal distribution of land cover classes

C. epigejos (40 %) and *P. australis* (22 %) cover most of the area followed by trees, bushes and the respective shadow with a spatial coverage of 19 %. Legume and non-legume herbs, mosses and lichens without or with a minor fraction of grass-like species cover 4.5 % and 4.8 % respectively. The remaining area was classified as *F. rubra* (LCC 8; 3.5 %). open water (3.1 %) and bare soil (2.6 %). The spatial coverage of each of the 16 LCCs is depicted in Fig. 4.
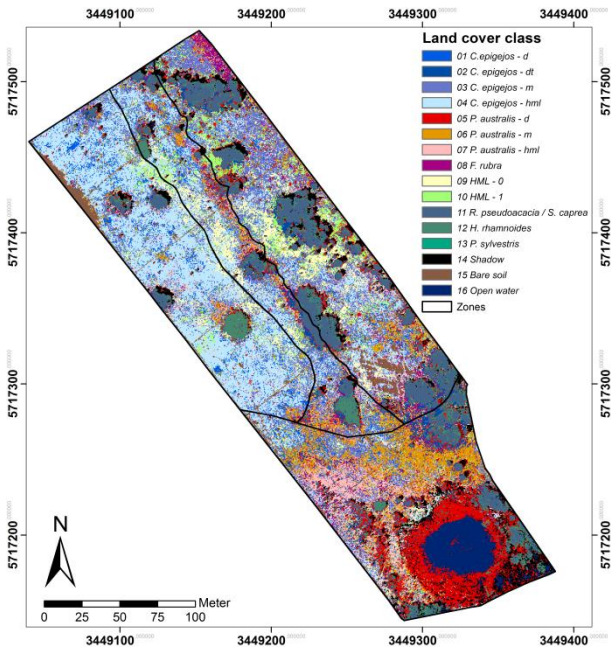
Figure 4: Spatial distribution of classified land cover classes (LCC).

The Si accumulators *C. epigejos* and *P. australis* showed a clear zonal distribution. *C. epigejos* was widespread in the northern zones of the catchment. Populations with high density (LCC 1 and 2) occurred regularly nearby the sunlit side of *R. pseudoacacia* (LCC 2). In reality, the populations were distributed more circular around the trees but the shaded side during image acquisition prevented from classification. Other high density populations (LCC 1) were predominately spread as smaller patches in the western zone. A clear zonal distinction could be observed for the two *C. epigejos* classes dominating the northern zones. The sparse populations (LCC 4) with a spatial coverage of 19 % occurred in the western zone and the central trench. LCC 3 as the second largest class (15 %) was widespread in the eastern zone and the central trench, but spatially separated by trees, bushes and larger patches of other LCCs (HML 0 and 1, bare soil). *P. australis* mainly occured in the southern zone of

the catchment with a dense population concentrated around the artificial pond. A narrow band run from the north-west to the south-east along the central trench. The less dense and the sparse populations (LCCs 6 and 7) occurred in a band-like pattern running in west-east direction. The zonal pattern reflected mainly wetter areas, i.e. the pond's fringe or sites where lateral groundwater flow approached the surface (return flow). The narrow NW-SE band marked the edge of an erosion gully along the central trench and the W-E band matched the belowground clay dams, where groundwater flow was forced towards the land surface.

3.3 Ground-based measurements of above ground biomass of *C. epigejos* and *P. australis*

With the exception of the separately sampled litter the variation of fresh shoot biomass was larger than the respective variation at *P. australis* sites (Table 2). The lowest amount was sampled at plot I5-2 with 126 g m^{-2}. In contrast, amounts at plot CA-1 were eight times higher (1018 g m^{-2}). Since the sampled litter was predominately dead material, differences between fresh and dry samples were naturally small. However, the overall variance was similar to that of fresh and dry shoot biomass but it should be noted that no correlation existed between the two quantities. High amounts of litter were sampled at plots with low and high shoot biomass (e.g. I5-2 and CA-2 respectively). The variation between the three plots at one site reflected the small-scale variability of the island-like populations of *C. epigejos* with decreasing shoot biomass from the center to the margins. While amounts at L2-3 (center) were 1.5 times higher than at L2-2 (margin) the factor increased to almost 3 between plots I5-3 and I5-2. The separately sampled litter varied within a range between 14 g m^{-2} (L2-1) and 126 g m^{-2} (I5-3).

Table 2: Mean, standard deviation (SD), min, max and Coefficient of Variation (CV) calculated for fresh and dry biomass samples of *C. epigejos* and *P. australis*.

	C. epigejos (n = 15)				*P. australis* (n = 9)			
	Fresh		Dry		Fresh		Dry	
	green shoot	litter	green shoot	litter	green shoot	litter (incl. brown shoot)	green shoot	litter (incl. brown shoot)
Mean	387	84	214	78	456	634	204	482
Sd	243	39	131	36	262	332	120	310
Min	126	14	57	13	133	251	50	178
Max	1018	150	465	139	830	1337	384	1106
CV [%]	63	47	61	47	58	52	59	64

Since there was no access to the dense *P. australis* population in the surrounding of the pond, highest and lowest amounts of fresh and dry shoot biomass were collected at site Q5. The small-scale variability in fresh green shoot biomass (factor 4.9) was even higher compared with *C. epigejos*. The fresh and dry samples of litter showed a high variance indicated by a CV of 74 % between plots. Again lowest and highest amounts were sampled at site Q5 with fresh weights of 57 g m^{-2} at Q5-2 and 646 g m^{-2} at Q5-1.

3.4 VI performance

All relationships calculated for the combinations between NDVIs and ground measured biomass showed a positive linear trend. The low NDVI values, ranging between 0.08 (*C. epigejos*; L2-2; $NDVI_{b891}$) and 0.41 (*P. australis*; P3-2; $NDVI_{b856}$) indicated no saturation effects. The respective R²s, Root Mean Square Errors (RMSE) [g m^{-2}] and Mean Relative Errors (MRE)
310 [%] for the examined relationships are summarized in Table 3.

Regarding the band combinations the NDVI using the RE b_{713} (Fig. 5) was found the best predictor for both species as well as for fresh green shoot biomass (Fig. 6a) and for the sum of fresh green shoot biomass and fresh litter (Fig. 6b). In both cases high R²s could be observed for *C. epigejos* (R² = 0.87) and *P. australis* (R² = 0.74 and R² = 0.78 respectively). While the other band combinations performed well for *C. epigejos*, the predictive power decreased significantly for *P. australis* (R²s range
315 between 0.40 and 0.11). VIs of *P. australis* showed higher values at same fresh green biomass amounts and generally a larger scatter of values than of *C. epigejos*. This effect was related to the different plant architecture of the two species. The combination of broader green leaves and larger but less individual plants of *P. australis* led to higher VIs representing the same biomass On the other hand, the number of pixel affected by shadow with decreasing population densities increased the scatter of VI values.

320 **Table 3: R², RMSE and MRE for relationships between examined NDVIs and aboveground biomass of *C. epigejos* and *P. australis*.**

	fresh green shoot biomass						fresh green shoot biomass plus litter					
	C. epigejos			*P. australis*			*C. epigejos*			*P. australis* (litter incl. brown shoot)		
Band	R²	RMSE	MRE	R²	RMSE	MRE	R²	RMSE	MRE	R²	RMSE	MRE
		[g m^{-2}]	[%]		[g m^{-2}]	[%]		[g m^{-2}]	[%]		[g m^{-2}]	[%]
b_{713}	0.87	84	27.3	0.74	126	38.5	0.87	89	19.5	0.79	353	31.3
b_{861}	0.82	100	29.2	0.37	197	55.3	0.81	106	20.9	0.36	389	30.0
b_{899}	0.82	99	31.6	0.33	202	60.6	0.80	108	23.1	0.40	376	29.1
b_{953}	0.73	123	36.6	0.11	234	76.6	0.70	132	27.1	0.21	434	39.7
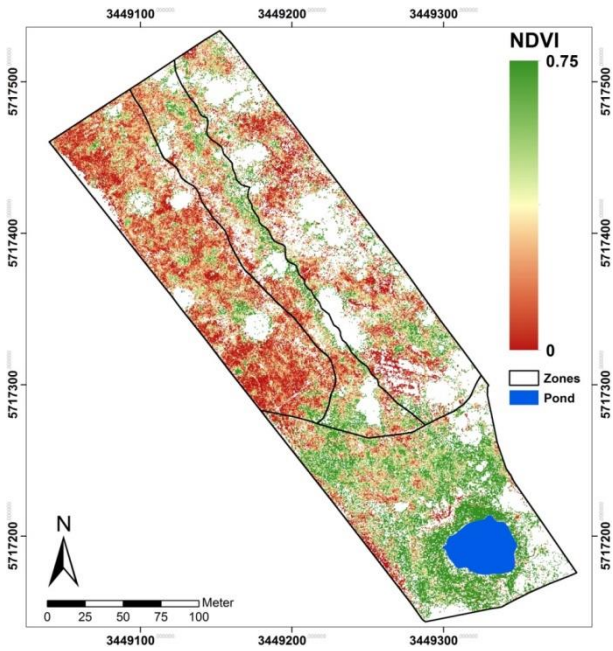
Figure 5: NDVI$_{b713}$ calculated from Eq. 1 using the red edge band. The area corresponds with the classified spread of *C. epigejos* (LCCs 1 – 4) and *P. australis* (LCCs 5 – 7).
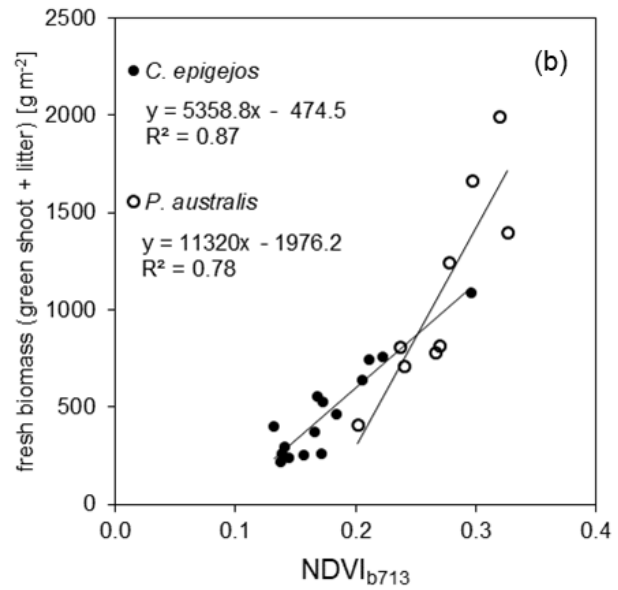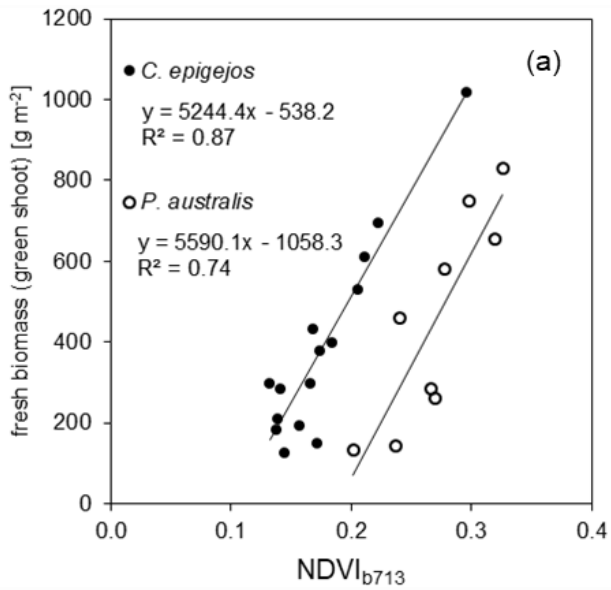
Figure 6: Respond of NDVIb713 to fresh green shoot biomass (a) and the sum of fresh green shoot biomass and litter (b) of *C. epigejos* and *P. australis*.

3.5 Estimation of dry biomass fractions

Taking into account the results of section 3.3, dry green shoots and the sum of dry green shoots and litter were calculated separately for each species. The quantities were highly correlated with R²s of 0.88 and 0.86 for *C. epigejos* and 0.99 and 0.97 for *P. australis*. The respective linear regressions (Fig. 7a and 7b) were used to model their spatial distribution in a first step. In a second step, the modelled amounts of dry green shoots were subtracted from the modelled sum of dry green shoots and litter to yield the spatial distribution of dry litter.
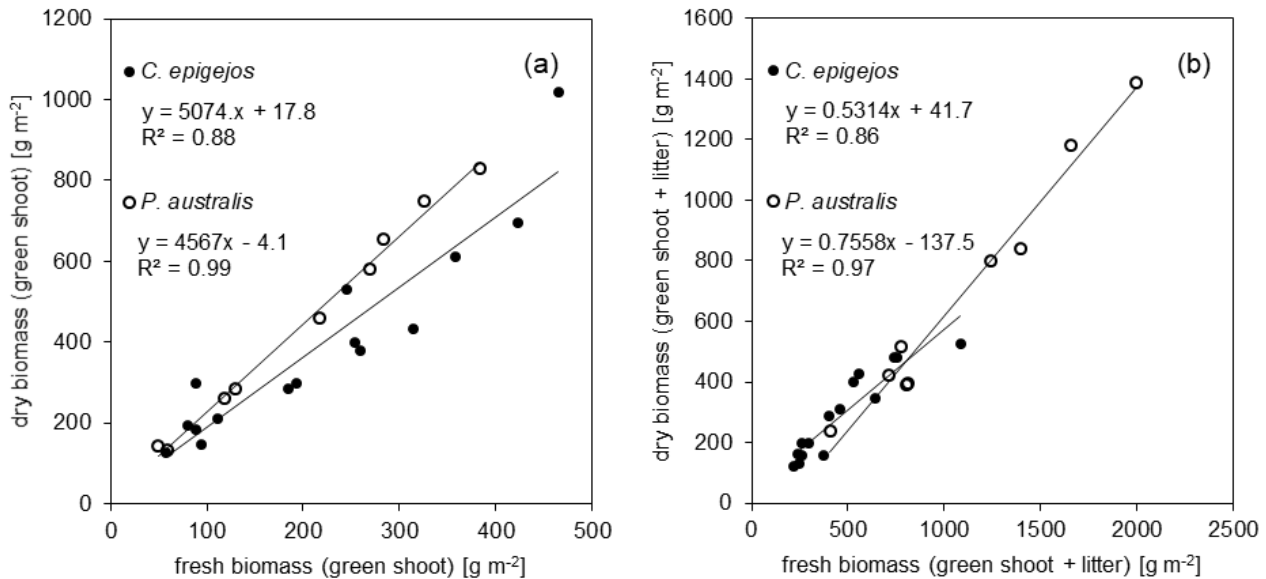
Figure 7: Correlation between fresh and dry green shoot biomass (a) and the respective biomass including litter (b) for *C. epigejos* and *P. australis*.

3.6 Silicon content and stocks of *C. epigejos* and *P. australis*

The mean Si content within dry litter of *C. epigejos* (3.7 %) was 1.8 times higher than the Si content in the dry shoot biomass of the current year (2.1 %). The effect was less pronounced for the three analyzed fractions of *P. australis* (Table 4). The Si content range between 3.0 % (dry litter without dry brown shoot biomass), 2.5 % (dry brown shoot biomass) and 2.3 % (dry green shoot biomass). As we regarded the sum of the first two fractions as litter, the mean of both contents (2.7 %) was used for further calculations. The mean fairly represented real conditions since both fractions, on average, contributed to the sum in equal amounts. Finally, the respective Si content was used to calculate the Si stocks in both fractions of *C. epigejos* and *P. australis*. The areas given in Table 4 equal the summed areal coverage of the classified LCCs 1–4 (*C. epigejos*) and 5–7 (*P. australis*). The total Si stock (sum of green shoot biomass and litter) accumulated in *P. australis* contributed to 64 % (275 kg) to the total Si stock calculated for the whole catchment (429 kg) despite the fact that the areal coverage was almost half that of *C. epigejos*.

Table 4: Mean Si content of biomass fractions of *C. epigejos* and *P. australis* and respective Si stocks calculated from the areal coverage derived from ML classification.

		Si content [%]		Si stocks		
	Fractions	Mean	CV [%]	[g m^{-2}]	Area [m²]	Si [kg]
C. epigejos	shoot biomass	2.1 (0.7)	33	6.0	20755	125
n = 15	litter	3.7 (1.0)	27	1.4		30
	total			7.4		155
P. australis	shoot biomass	2.3 (0.4)	17	7.5	10063	75
n = 9	litter	2.7 (0.4)	13	19.8		199
	total			27.3		274
Catchment				13.9	30818	429

This was simply caused by the fact that *P. australis* formed more dry biomass per unit ground area than *C. epigejos* (factor 2.3 on average). The spatial distribution of total Si stocks calculated on the basis of the real areal coverage of both species is depicted in Fig. 8a and Fig. 8c. According the higher biomass production, Si stocks of *P. australis* reached a maximum (98 g m^{-2}) in the fringe around the pond. The majority between 3 g Si m^{-2} and 60 g Si m^{-2} occurred in the southern zone and in a narrow band along erosion gullies in the central trench.
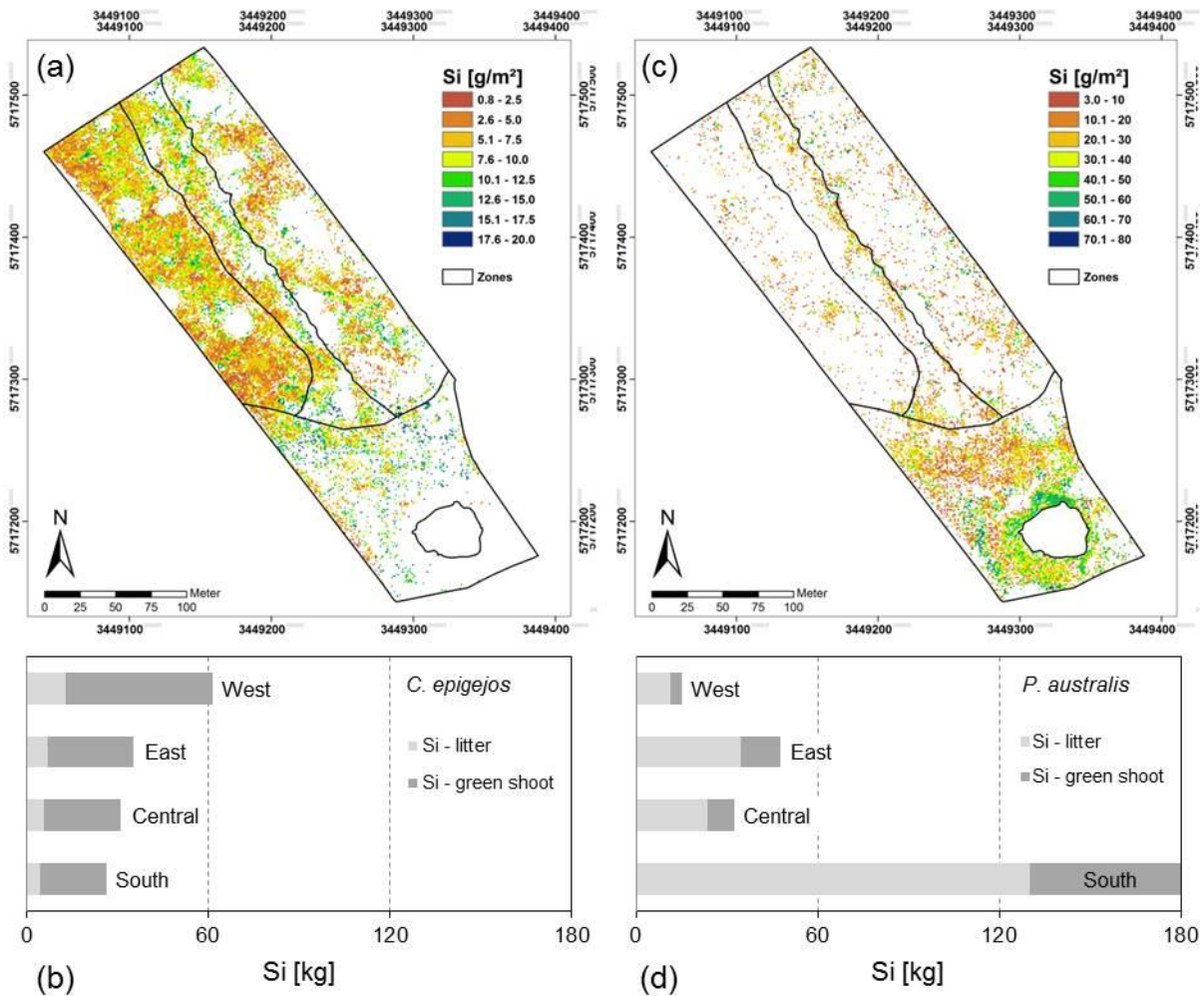
Figure 8: Spatial distribution of Si stocks of *C. epigejos* (a) and *P. australis* (c) and total amounts of Si accumulated in the four zones by *C. epigejos* (b) and *P. australis* (d). Note the different legend scales in (a) and (c).

With the exception of few patches in the southern zone the vast majority of values did no not exceed 17 g m^{-2} in the case of *C. epigejos*. It is noticeable that the southern zone showed a clear two-parted internal zonation. The northern part was a type of a transition zone showing a co-occurrence of both species with high Si accumulation in *C. epigejos*, whereas the southern part was dominated by *P. australis* in the surrounding of the pond. This indicated that the spatial pattern was caused by soil moisture conditions rather than the initial spatial differences in soil properties induced by construction work and explained the relative low zonal contribution of 17% (26 kg) to the total Si stock of 154 kg (Fig. 8b).

Regardless the accumulated Si in the southern zone and the central trench, the clear distinction between the eastern and western zone was striking. While the western zone contributed to 40% (62 kg), only 23% (35 kg) were accumulated in the eastern zone. Values corresponded to mean Si stocks of 4.0 g m^{-2} and 2.3 g m^{-2} respectively.

Figure 8d shows the Si stocks accumulated in *P. australis* calculated for each of the four zones. While the southern zone contributed to 66 % (180 kg Si) to the total amount, Si stocks in northern zones played a minor role. Mean Si stocks reached 12.2 g Si m^{-2} in the southern zone but significantly lower values in the eastern (3.1 g Si m^{-2}) and the western zone (1.0 g Si m^{-2}). Although mean Si stocks in the central trench were similar to those in the eastern zone (3.6 g Si m^{-2}) the occurrence of *P. australis* tended to be more linear along the main gully. Regarding habitat requirements of *P. australis*, the occurrence was a result of higher soil moisture conditions in this area and the partially wet and flooded sites around the pond.

3.7 Relationship between Si stocks of *C. epigejos*, *P. australis* and site properties

From a total of 124 grid points we excluded all locations in the central trench due to disturbances in soil properties and related nutrient availability caused by water erosion compared to the initial conditions in 2005. Moreover, we excluded several grid points within the remaining zones located below trees and bushes without any classified occurrence of *C. epigejos* and *P. australis*. Finally, Si stocks and site properties of 35 grid points located in the western, 32 in the eastern and 18 in the southern zone were used for statistical analysis. Mean Si stocks were extracted from a squared area of 25 m² around each grid point.
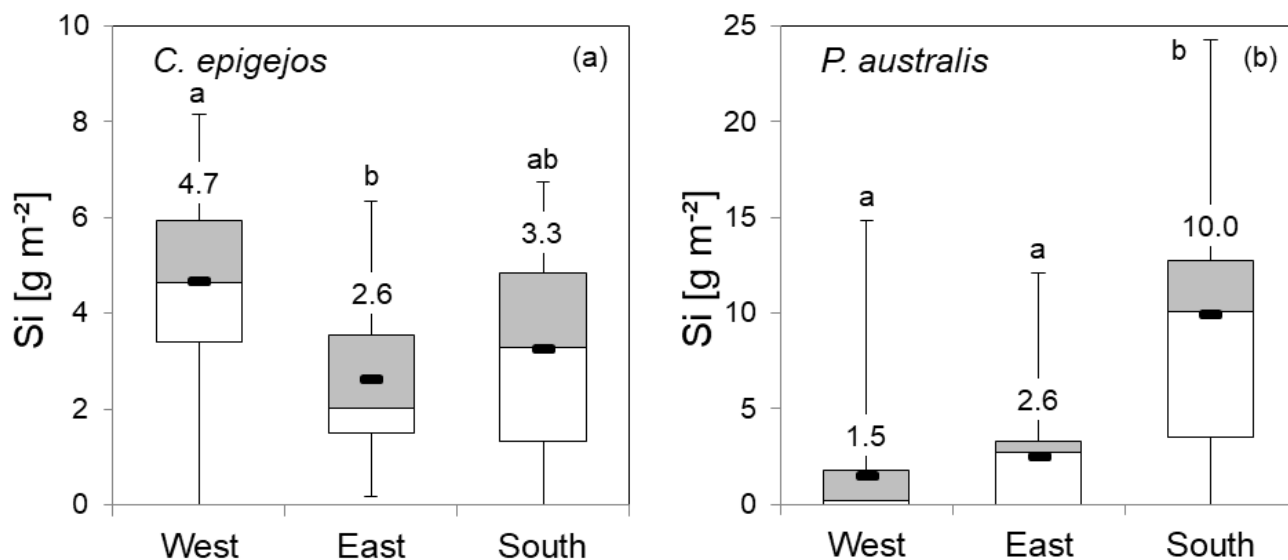
Figure 9: Si stocks of *C. epigejos* (a) and *P. australis* (b) at grid points in the western, eastern and southern zone. Numbers represent zonal means (box plots: mean, upper and lower quartile, minimum and maximum). Letters (a and b) indicate statistical significance of differences between zones according to Kruskal-Wallis ANOVA (p < 0.05). Note the different scaling of the y-axes.

Compared to the zonal means of 4.0 g m^{-2}, 2.3 g m^{-2} and 1.8 g m^{-2} for *C. epigejos*, the Si stocks extracted at grid points increased to 4.7 g m^{-2} in the western, 2.6 g m^{-2} in the eastern and 3.3 g m^{-2} in the southern zone (Fig. 9a). However, the ratios of 0.9 for the western and eastern zone indicated an adequate representation of the grid points for both zones. The large difference in the southern zone was mainly caused by the two-parted zonation with almost no occurrence of *C. epigejos* in

more than half of the southern zone area. Zonal Si stocks accumulated in *P. australis* in the western, eastern and southern zone (1.0 g m⁻², 3.1 g m⁻² and 12.2 g m⁻²) were sufficiently represented by grid points in all zones (1.5 g m⁻², 2.6 g m⁻² and 10.0 g m⁻²) (Fig. 9b). According to Kruskal-Wallis ANOVA ($p < 0.05$), differences in mean Si stocks were statistically significant between the western and eastern zone for *C. epigejos* and between the southern and the other two zones for *P. australis*. Among the examined soil properties, means of clay content (Fig. 10a) showed a corresponding trend with respect to Si accumulation in dry biomass of *C. epigejos* for all three zones including the significant difference between the western and eastern zone ($r_s = 0.385$, $p = 0.001$).
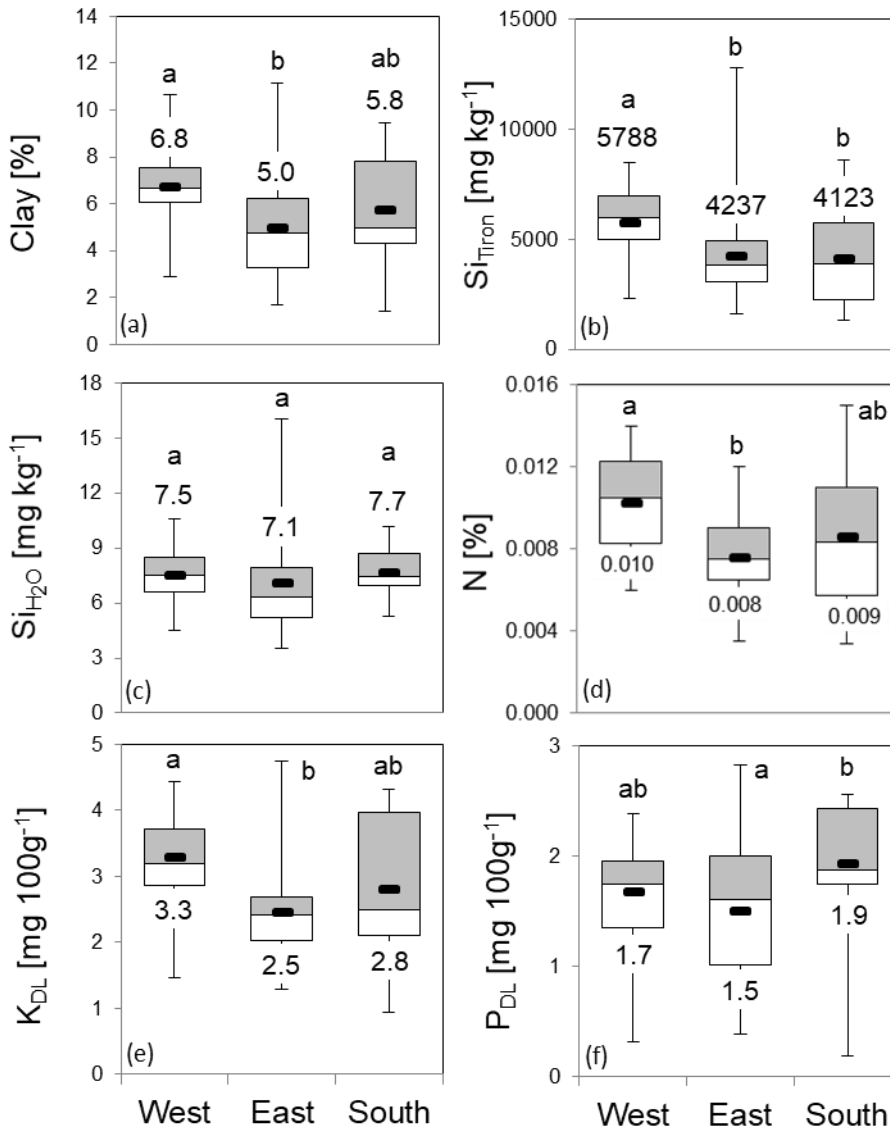
Figure 10: Soil properties and nutrients at grid points in the western, eastern and southern zone (box plots: mean, upper and lower quartile, minimum and maximum). Figures depict the distribution of clay content (a), Tiron extractable amorphous Si (SiTiron) (b), water soluble Si (Si – H_2O) (c), nitrogen (d), potassium (e), and phosphorus (f). Numbers represent zonal means. Letters (a and b) indicate statistical significance of differences between zones according to Kruskal-Wallis ANOVA (p < 0.05).

405

Significant differences were found for Si_{Tiron} (Fig. 10b) between the western and the eastern zone, whereas values in the southern zone did not differ very much from those in the eastern zone ($r_s = 0.416$, $p < 0.001$). The water soluble Si (Fig. 10c) could be ruled out as a driving factor since there was no differentiation between means over all zones ($r_s = 0.004$, $p = 0.971$).

410 The zonal distribution of the most important nutrients drew a similar picture. Highly significant differences of means between the western and eastern zone were found for nitrogen (Fig. 10d) and potassium (Fig. 10e). For both nutrients, slightly higher values compared to the eastern zone could be observed for the southern zone which is in accordance with higher Si stocks (N: $r_s = 0.412$, $p < 0.001$; K_{DL}: $r_s = 0.419$, $p < 0.001$). It can be concluded that P_{DL} is not a driving factor for the spatial spread of *C. epigejos* populations at chicken Creek, since availability was more or less equal in all three zones (Fig. 10f) ($r_s = -0.019$, $p =$

415 0.871).

As stated before, the occurrence of *P. australis* was governed mainly by soil moisture conditions. Therefore neither examined soil properties nor nutrient availability showed a recognizable impact on the spatial spread along zones. No significant correlations between Si stocks of *P. australis* and soil properties were detectable with the exception of Si_{Tiron} ($r_s = -0.307$, $p =$ 0.007).

420 **4 Discussion**

4.1. Aboveground phytogenic Si stocks at Chicken Creek

Mean aboveground Si stocks of *P. australis* and *C. epigejos* are surprisingly high and are comparable to or markedly exceed reported values for the Si storage in aboveground vegetation, e.g., in the Great Plains (short grass steppe and tall grass prairie, 2.2 to 6.7 g Si m^{-2}, Blecker et al., 2006), the tropical humid grass savanna (tall grass *Loudetia simplex*, 3.3 g Si m^{-2}, Alexandre

425 et al., 2011) or forested biogeosystems (beech forest: 8.3 g Si m^{-2}, Sommer et al., 2013; Beech-fir forest: 18 g Si m^{-2}, pine forest: 9 g Si m^{-2}, Bartoli, 1983). Maxima of Si stocks at Chicken Creek reach values (up to 98 g Si m^{-2}) that are comparable to the Si storage in wetlands (50 to100 g Si m^{-2}, Struyf and Conley, 2009). Due to the fact that the Si content of *C. epigejos* and *P. australis* are in line with published values for grasses in general (Hodson et al., 2005), we conclude the observed Si stocks to be predominantly driven by the (high) biomasses of both plants. If we assume a more or less steady annual Si

430 accumulation in *C. epigejos* for 5 years (*C. epigejos* became one of the most dominating plant species since 2010, Zaplata et al., 2011b), the mean Si accumulation in the aboveground biomass of *C. epigejos* amounted to about 6.0 g Si m^{-2} per year. If we further assume a similar time span for the Si accumulation in *P. australis*, the mean Si accumulation in the aboveground biomass of *P. australis* amounted to about 7.5 g Si m^{-2} per year. Thus, annual Si fixation in *C. epigejos* and *P. australis* at

Chicken Creek exceeds published data on annual biosilicification rates of temperate forest biogeosystems (beech forest: 3.5 g Si m^{-2} yr^{-1}, Sommer et al., 2013; Beech-fir forest: 2.6 g Si m^{-2} yr^{-1}, pine forest: 0.8 g Si m^{-2} yr^{-1}, Bartoli, 1983; Douglas fir forest: 3.1 g Si m^{-2} yr^{-1}, Norway spruce forest: 4.4 g Si m^{-2} yr^{-1}, black pine forest: 0.2 g Si m^{-2} yr^{-1}, European beech forest: 2.3 g Si m^{-2} yr^{-1}, oak forest: 1.9 g Si m^{-2} yr^{-1}, Cornelis et al., 2010).

In the light of potential aboveground biomasses of, e.g., *C. epigejos* (up to about 700 g m^{-2}, Rebele and Lehmann, 2001), our results emphasize the significance of grasses for Si cycling in general. In this context, eutrophication is one of the most important drivers of the increased abundance of *C. epigejos* in many regions of Central Europe, especially East Germany, Poland, and Czech Republic (Rebele and Lehmann, 2001), while on the other hand eutrophication might also be one of the drivers of the decline of *P. australis* in numerous European wetlands since the 1950s (Van der Putten, 1997). Considering the net primary production of the worldwide major biome types and the average amounts of Si fixed in the corresponding vegetation, the significance of grasses for Si cycling becomes much clearer: tropical woodland and savanna, temperate steppe, tundra, wetland, and cultivated land belong to the biome types where Si is actively accumulated and vegetation is widely dominated by grasses (Carey and Fulweiler, 2012). Humans directly affect the distribution and size of these biomes and thus influence corresponding Si cycling through intensified land use and management change in forestryand agriculture (Struyf et al., 2010, Vandevenne et al., 2015a, b). Si exports through harvested crops generally lead to a Si loss in agricultural used soils (= anthropogenic desilication) (Desplanques et al., 2006, Guntzer et al., 2012, Keller et al., 2012, Meunier et al., 2008, Vandevenne et al., 2012). These losses can be compensated by, e.g., the application of phytogenic Si in the form of biochar or crop straw recycling (Li and Delvaux, 2019; Yang et al., 2020; Puppe et al., 2021).On a global scale, field crops synthesize about 35 % of Si accumulated in vegetation and this proportion is going to increase with increased agricultural production within the next decades (Carey and Fulweiler 2016). In this context, targeted manipulation of Si cycling might be a promising strategy to enhance carbon sequestration in agricultural biogeosystems to mitigate climate change (Song et al., 2014).

4.2. Initial soil properties as drivers of spatial patterns of *C. epigejos* and *P. australis* and corresponding Si stocks

In general, the composition and structure of plant communities and the spatial distribution of plant biomass are mainly controlled by climatic, edaphic (e.g., soil moisture/texture, pH, and nutrients) and geographic-historic factors as well as by species interactions (e.g., consumption by herbivores) and anthropogenic perturbations (e.g., Polis 1999). At Chicken Creek consumption of plants by herbivores can be generally excluded, because the total study area is fenced. Studies of Zaplata et al. (2011a, 2013) indicated that differences in vegetation dynamics at Chicken Creek can be directly derived from slight differences in edaphic conditions resulting from construction work with large machines (Gerwin et al., 2010).

In this context, especially differences in soil pH, carbon content, calcium carbonate and conductivity between the sandier eastern and the loamier western part were identified to influence plant species distribution in general (Zaplata et al., 2013). Our results on hand generally corroborate this differentiation between zones of Chicken Creek with clay, N, K_{DL}, and Tiron extractable Si content as important drivers of the small-scale distribution of *C. epigejos*. Süß et al. (2004) analysed plant successional trajectories and corresponding drivers in calcareous sand ecosystems in the northern upper Rhine valley in

Germany. They found the successional trajectories of *C. epigejos* to be correlated to total N, extractable P and K as well as soil moisture. In contrast, the most important nutrients for aboveground biomass production of *C. epigejos* seem to be N and calcium, while P and K seem to have no significant effect on biomass production (Rebele and Lehmann, 2001). This also is in

470   line with our observation that P_{DL} seems to be no driver of the small-scale distribution of *C. epigejos* at Chicken Creek. Plant available Si concentrations seem to be no driver for the distribution of *C. epigejos* and *P. australis* as well. This might be a hint that Si accumulation in plants is probably more influenced by the phylogenetic position of a plant than by environmental factors like temperature or Si availability (cf. Prychid et al., 2004, Hodson et al., 2005, Cooke and Leishman 2012).

4.3. Benefits and limitations of UAS-based remote sensing of phytogenic Si stocks

475   Natural ecosystems are characterized by an abundant flora, arranged in a complex spatial pattern. Despite the use of ultrahigh resolution UAS imagery, a sufficient classification of all relevant species in an ecosystem is challenging or even impossible and has been addressed in previous studies (e. g. Dunford et al., 2009; Laliberte et al., 2011; Husson et al., 2016). While larger individuals like trees and bushes are easy to identify, the size of the majority of species at Chicken Creek is far below the 10 cm spatial resolution of the multispectral imagery used in our study and tall growing plants or broad leaved

480   species prevent the sensor of seeing low growing species below. Consequently, and in contrast to the classification of monocultures, the produced LCC map of the Chicken Creek catchment merely represents the spatial distribution of species or species compositions visible to the sensor. For this reason, we could hardly use the botanical mapping at grid points provided by M. Zaplata to validate our classification but we could use these data as a rough quality check. Hence, training areas for the classification have been defined giving priority to the two main Si accumulators under study. However, both limitations were

485   of minor importance in the case of *P. australis* and *C. epigejos*. Even smaller patches of both species were large enough to be identified unless the spatial resolution. With the exception of the transition zone northeast of the pond, where *C. epigejos* co-exist below *P. australis*, populations are spatially separated and represent the uppermost layer of the canopy within the respective plant community. This may lead to slight underestimations of the spread of *C. epigejos* and the subsequently estimated Si – stock in this area. The clear spectral distinction between similar signatures prevents many other species from

490   proper classification in general and in particular in the case of only few available spectral bands. This limitation can be diminished by choosing an appropriate date for image acquisition, when the predominately green leaves of *C. epigejos* and *P. australis* enhance the optical contrast against the background reflectance of herbs, mosses and lichens. This cannot avoid the inclusion of other grass-like species such as *F. rubra* or *B. sylvaticum* in one of the *C. epigejos* or *P. australis* classes and the confusion with litter in case of sparse vegetation cover.

495   The majority of studies using the original NDVI, other VIs or combinations of VIs have been derived from satellite imagery at landscape level (e. g. short grass prairie, Anderson et al., 1993; short grass steppe, Todd et al., 1998; rangeland, Mundava et al., 2014; different types of grassland and temperate steppe, Meng et al. 2018) showing poor up to moderate correlations between VIs and above ground biomass. R²s range between 0 and 0.6 for either total biomass or fractions of biomass caused

by insufficient spatial and spectral resolution but mainly by background reflectance of soil, shadow or non-photosynthetic plant components such as standing dead plants or litter. The immense quantity of studies which evaluated different sensors with numerous VIs at various scales and environments hamper a clear assessment of our results. While several studies reported no or minor improvements in the relationships between red edge VIs involving the wavelength region between 680 nm to 750 nm and vegetation parameters (e. g. Cui and Kerekes, 2018; Easterday et al., 2019), other studies carried out over heterogeneous forest stands have proven the red edge reflectance to be sensitive to chlorophyll content while largely unaffected by structural properties and crown shadow (e.g. Zarco-Tejada et al., 2018, Xu et al., 2019). This explains in parts the outperformance of our results compared to the aforementioned studies and the results presented here, in particular for *P. australis*, which show a drastic decrease of R^2s when NIR reflectance bands where used instead of the red edge band. The most important benefit of UAS remote sensing of phytogenic Si stocks is its potential to cover the heterogeneity in plant biomasses and thus phytogenic Si stocks. This is in contrast to previous studies, which assumed identical biomasses for Si stock quantifications (e.g., Cornelis et al., 2010; Sommer et al., 2013; Turpault et al., 2018). In addition, these studies mainly focused on a single plant species in a given ecosystem. Contrary, UAS remote sensing enables to detect biomasses of different plant species simultaneously, and thus to quantify Si stocks in a lifelike way. Furthermore, UAS remote sensing enables the detection of plant biomasses in larger areas, i.e., at a landscape scale, which is also in contrast to previous studies, which used results of small study plots for an extrapolation to larger spatial units up to a global scale implicitly assuming similar environmental conditions (e.g., Carey and Fulweiler, 2012). Due to the fact that aboveground biomass of plants seems to be the main factor of corresponding phytogenic Si stock quantities (the variations in Si content in a plant species in a given ecosystem are considerably lower, especially when we assume that the phylogenetic position of a plant - rather than environmental factors - determines potential plant Si content, see, e.g., Hodson et al. 2005), a detection of biomass heterogeneities via UAS remote sensing represents a promising tool for the quantification of lifelike phytogenic Si pools at landscape scales.

As both species, *C. epigejos* as well as *P. australis*, analysed at Chicken Creek show a wide range of biomass (0.1 - 98 g m-2), the use of mean biomasses in Si stock calculations or Si cycling models generally leads to deviations, thus substantial Si stock underestimations or overestimations. For a profound understanding of Si cycling in general and the influence of land use in particular, detailed information on the small-scale spatial distribution of plant related Si stocks based on an accurate biomass assessment is urgently needed. This information will help us to understand the interaction between edaphic factors, plant distribution, ecosystem productivity (biomass), and anthropogenic desilication on a local (i.e. site-specific) scale. Due to the fact that ultrahigh resolution imagery captured by UASs is capable of differentiating between Si accumulating species and respective fresh biomass and litter, this technique is also a promising tool for the detailed assessment of Si fluxes in grasslands. As Si content of litter have been recognized as an important driver of decomposition rates (Schaller et al., 2016, 2017), information on litter Si stocks will further help us to better understand ecosystem biogeochemistry in general.

5 Conclusions

We found mean aboveground Si stocks of *P. australis* and *C. epigejos* to be comparable to or even distinctly higher than reported values for the Si storage in aboveground vegetation of different terrestrial biogeosystems. Biomasses of both plants were quite high and have been found to be the main driver of Si stocks at Chicken Creek as Si concentrations of *C. epigejos* and *P. australis* were in line with previously published values.

From our results we can conclude that the distribution of *C. epigejos* and *P. australis* and corresponding Si stocks at Chicken Creek is clearly determined by initial soil properties. While we found clay, N, K_{DL}, and Tiron extractable Si contents to be important drivers of the small-scale distribution of *C. epigejos*, the distribution of *P. australis* was mainly governed by soil moisture conditions. For the distribution of both grasses and corresponding Si stocks we found no relation to plant available Si concentrations in soils. This supports our findings that biomasses are the main drivers of Si stocks at Chicken Creek.

The UAS-based remote sensing of phytogenic Si stocks exhibits several benefits: (i) the heterogeneity in plant biomasses and corresponding Si stocks can be covered, (ii) biomasses of different plant species can be detected simultaneously, and (iii) plant biomasses in larger areas, i.e., at a landscape scale, can be captured. However, UAS-based remote sensing of phytogenic Si stocks is aggravated by some technical limitations (e.g., the spatial resolution of the multispectral imagery) that have to be considered during the interpretation of results.

Appendix A

Appendix A1: UAS, camera specification, and mission settings

The Carolo P360 is a fixed wing construction, developed by the Institute of Aerospace Systems of the Technical University Braunschweig (Fig X). With a wingspan of 3.6 m and a take-off weight of almost 22.5 kg including the complete battery set for the electric drive motor, the MINC autopilot system including servo actuators and the payload (sensors and control unit), the UAS is capable to carry an additional payload of approximately 2.5 kg. The battery set allows flight durations of approximately 40 min at ground speeds between 20 m s^{-1} and 30 m s^{-1} including the time for climbing and landing.

The multispectral camera Mini-MCA 12 is a compact modular construction integrating two basic modules into one rugged chassis. Each module consists of an array of six individual CMOS sensors (1280 × 1024 pixels; pixel size 5.2 µm), lenses (focal length 8.5 mm) and mountings for user definable band-pass filters. The filter configuration and specific properties are summarized in Table A1.

Mission settings followed the recommended cruising speed of 25 m s^{-1} and the camera exposure time of 2 s resulted in an overlap in flight direction of approximately 50%. A distance of 40 m between the flight paths required to achieve a sufficient across flight overlap of at least 60%. Twenty-two waypoints were predefined, each marking a start- and endpoint of 10 parallel flight paths with a total length of 8.6 km including the loop lines. In order to maintain the GSD of ~ 0.1 m, terrain effects were compensated by setting the flight altitude to 163 m for the northern- and 153 m for the southern waypoints. A total of 2556 individual (≙ 213 multispectral) images were captured during the mission.

565 **Table A1: Filter configuration of the Mini-MCA 12 and optical properties of the mounted filters. For band 2 (b) no fact sheet has been provided.**

Band	Center Wavelength [nm]	FWHM* Coordinates (Bandwidth) [nm]	Bandwidth (10%) [nm]	Peak Transmission [%]
1	471	466.0 – 475.1 (9.1)	12.8	68.3
2	515	N/A (≈10.0)	N/A	N/A
3	551	545.5 – 555.6 (10.1)	14.8	56.4
4	613	607.7 – 617.8 (10.2)	14.2	67.6
5	658	653.4 – 662.9 (9.5)	13.6	69.2
6	713	708.1 – 717.7 (9.6)	13.4	63.0
7	761	756.2 – 766.7 (10.5)	14.7	71.9
8	802	797.3 – 807.3 (10.1)	14.5	56.3
9	831	826.3 – 835.8 (9.5)	13.1	55.3
10	861	856.4 – 866.4 (10.1)	14.0	64.2
11	899	891.3 – 907.7 (16.4)	22.9	63.6
12	953	933.0 – 973.8 (40.8)	58.2	69.6

Appendix A2: Image post-processing chain

Post-processing of MCA imagery aimed at the conversion of raw digital numbers (DN) into georeferenced at-surface

570 reflectance images. This multistage procedure consisted of three major components (i) radiometric image correction and (ii) transformation of sensor coordinates into a geographic coordinate system and image alignment and (iii) absolute radiometric calibration. The radiometric image correction included periodic and checkered pattern noise reduction, correction of sensor-based illumination fall-off (vignetting), horizontal band noise removal (caused by the progressive shutter of CMOS sensors) and lens distortion. The transformation of sensor coordinates included the fusion of recorded GPS measurements with collected

575 images, band-wise automated aerial triangulation (AAT), the minimizing of remaining geometric distortions and the alignment of single bands to one multispectral image using ground control points (GCPs). Due to homogenous environmental conditions during the 10 minutes of image acquisition (weather and illumination geometry), we renounced the conversion of measured DNs into at-surface reflectance, which is required for the retrieval of physical parameters of vegetation canopies or bare soil properties because a recorded DN is not only a function of the spectral characteristics of vegetation or soils but also of

580 environmental condition (Moran et al., 1995). A detailed description of the multistage procedure is beyond the scope of this paper. Thus the following paragraphs give a brief overview of the basic methods used in this study to generate one georeferenced multispectral image from the recorded raw images.

Radiometric corrections comprised noise reduction, correction for vignetting and lens distortion effects. The dark offset subtraction technique proposed by (Kelcey and Lucieer, 2012) reduced the noise component of an image by subtracting the

585 average per-pixel noise calculated from 120 repetitions captured in a completely darkened environment for each of the 12 sensors. The method used for the correction of vignetting effects basically uses a look-up table (LUT) for each sensor, composed of correction factors for each pixel derived from flat field imagery (Mansouri et al., 2005). These were generated by capturing multiple images of an evenly illuminated white cardboard with almost lambertian properties and constant spectral characteristics over VIS and NIR wavelengths. In a first step the per-pixel average and the corresponding standard deviation

590 were calculated from a total of 10 images for each of the 12 sensors at different exposure levels, followed by a subtraction of the respective dark offset imagery.

To account for the horizontal band noise induced by the progressive shutter of the camera, a shutter correction factor was calculated (Wehrhan et al., 2016).

Finally, a correction technique for lens distortions was applied. The plumb-line approach described in the Brown–Conrady model

595 (Hugemann, 2010) is implemented in the PhotoScan-Pro V.1.7. software (Agisoft LLC, St. Petersburg, Russia). The model required the input of the focal length (8.5 mm) and the pixel size (5.2 µm). Internal and external orientation of each camera (band) were then estimated automatically from the geometry of an image sequence during the image alignment process (Dall'Asta and Roncella, 2014). Mosaicking and geo-referencing using The PhotoScan-Pro workflow involved common photogrammetric procedures including the search for conjugate points by feature detection algorithms used in the bundle adjustment procedure,

600 approximation of camera positions and orientation, geometric image correction, point cloud and mesh creation, automatic georeferencing and finally the creation of an orthorectified mosaic (Conçalves and Henriques, 2015). This workflow was applied to each of the 10 bands independently. The ERDAS Imagine software (Hexagon Geospatial, Norcross, GA, U.S.) was then used to improve the spatial accuracy and to transform the single bands to the local coordinate system ETRS 89 UTM 33 by using the precisely measured raster point coordinates. Finally the 10 bands were stacked to a single multispectral image.

605 For more details regarding description of methods, used materials and technical equipment the reader is referred to Wehrhan et al., 2016.

Appendix B

Appendix B1: Image Classification

A supervised pixel-based classification of a natural ecosystem needs a clear understanding of the nature and the expected

610 results. The result is governed (i) by the spectral and spatial resolution of input imagery, (ii) the biodiversity, (iii) the morphology of the vegetation layer and (iiii) the selection of adequate training areas. The ultrahigh resolution easy allowed the identification of larger objects such as trees, patches of bare soil and some individuals of *P. australis* but was still too low to identify individuals of *C. epigejos*. Due to almost unique spectral properties of green grass-like species, the number and the bandwidths of spectral MCA bands was insufficient for a clear distinction. The morphology of the vegetation layer determined

whether a species is visible to the sensor or hidden by another species, e.g. trees or *P. australis* plants prevent the classification of an underneath growing *C. epigejos* population. Finaly, the selection of training areas determined the classification quality. Selecting small training areas with little statistical variation in the signatures may result in large unclassified areas and vice versa. The separabilty between classes will be diminished if the signatures of the respective training areas are to some extent similar. As it is typical for a supervised maximum-likelihood classification, several trials were necessary to define an appropriate number of representative training areas with sufficient statistical separabilty of signatures. Taking all aforementioned aspects into account, class definition was driven by the objectives addressed in this particular study. We are aware that these classes in parts do not coincide with vegetation or species communities as they are defined in the terminology of ecologist or biologists. However, for simplification purposes the term land cover class (LCC) was used.

Author contribution

Conceptualization: M.S.; Formal analysis: M.W., D.P. and D.K.; Funding acquisition: M.S.; Investigation: M.W., D.P. and D.K.; Methodology: M.W. and M.S.; Project administration: M.S.; Resources: M.S.; Validation: M.W., D.P, D.K. and M.S.; Visualization: M.W.; Writing - original draft preparation: M.W., D.P. and M.S.; Writing – review & editing: M.W., D.P. and M.S..

Competing interests

The authors declare that they have no conflict of interest.

Acknowledgements

This study has been financed by the Deutsche Forschungsgemeinschaft (DFG) under grant SO 302/7-1 (*Spatiotemporal dynamics of biogenic Si pools in initial soils and their relevance for desilication*). D.P. was funded by the Deutsche Forschungsgemeinschaft (DFG) under grant PU 626/2-1 (*Biogenic Silicon in Agricultural Landscapes (BiSiAL) – Quantification, Qualitative Characterization, and Importance for Si Balances of Agricultural Biogeosystems*).

References

Alexandre, A., Meunier, J. D., Colin, F., and Koud, J. M.: Plant impact on the biogeochemical cycle of silicon and related weathering processes, Geochimica et Cosmochimica Acta 61, 677-682, 1997.

Alexandre, A., Bouvet, M., and Abbadie, L.: The role of savannas in the terrestrial Si cycle: a case-study from Lamto, Ivory Coast, Global and Planetary Change 78, 162-169, doi: 10.1016/j.gloplacha.2011.06.007, 2011

Anderson, G. L., Hanson, J. D., and Haas, R. H.: Evaluating Landsat Thematic Mapper derived vegetation Indices for estimating above-ground biomass on semiarid rangelands, Remote Sens. Environ., 45, 165-175, doi: 10.1016/0034-4257(93)90040-5, 1993.

Barão, L., Clymans, W., Vandevenne, F., Meire, P., Conley, D. J., and Struyf, E.: Pedogenic and biogenic alkaline-extracted
645   silicon distributions along a temperate land-use gradient, Eur. J. Soil Sci. 65, 693-705, doi: 10.1111/ejss.12161, 2014.

Baret, F. and Guyot, G.: Potentials and limits of vegetation indices for LAI and APAR assessment, Remote Sens. Environ.,
35, 161-173, doi: 10.1016/0034-4257(91)90009-U, 1991.

Bartoli, F.: The biogeochemical cycle of silicon in two temperate forest ecosystems, Environ. Biogeochem. Ecol. Bull., 35,
469-476, doi: 10.1016/j.gca.2007.11.010, 1983.

650   Berni, J. A. J., Zarco-Tejada, P. J., Suárez, L., and Fereres, E.: Thermal and Narrowband Multispectral Remote Sensing for
Vegetation Monitoring From an Unmanned Aerial Vehicle, IEEE Trans. Geosci. Remote Sens., 47, 722-738, doi:
10.1109/TGRS.2008.2010457, 2009.

Biermans, V. and Baert, L.: Selective extraction of the amorphous Al, Fe and Si oxides using an alkaline Tiron solution, Clay
Miner., 12, 127-135, doi: 10.1180/CLAYMIN.1977.012.02.03, 1977.

655   Blecker, S. W., McCulley, R. L., Chadwick, O. A., and Kelly, E. F.: Biologic cycling of silica across a grassland
bioclimosequence, Global Biogeochemical Cycles, 20, doi: 10.1029/2006GB002690, 2006.

Bouman, B. A. M.: Accuracy of estimation the leaf area index from vegetation indices derived from crop reflectance
characteristics, a simulation study, Int. J. Remote Sens., 13:16, 3069-3084, doi: 10.1080/01431169208904103, 1992.

Broge, N. H. and Leblanc, E.: Comparing prediction power and stability of broadband and hyperspectral vegetation indices
660   for estimation of green leaf area index and canopy chlorophyll density, Remote Sens. Environ., 76, 156-172, doi:
10.1016/S0034-4257(00)00197-8, 2000.

Carey, J. C. and Fulweiler, R. W.: The terrestrial silica pump, PLoS One 7, doi: 10.1371/journal.pone.0052932, 2012.

Carey, J. C. and Fulweiler R. W.: Human appropriation of biogenic silicon–the increasing role of agriculture, Functional
Ecology, 30, 1331-1339, doi: 10.1111/1365-2435.12544, 2016.

665   Ciu, X., Gibbes, C., Southworth, J., and Waylen, P.: Using Remote Sensing to Quantify Vegetation Change and Ecological
Resilience in a Semi-arid System, Land, 2, 108-130, doi: 10.3390/land2020108, 2013.

Clarke, J.: The occurrence and significance of biogenic opal in the regolith, Earth-Sci. Rev., 60, 175-194, doi: 10.1016/S0012-
8252(02)00092-2, 2003.

Clymans, W., Struyf, E., Govers, G., Vandevenne, F., and Conley, D.J.: Anthropogenic impact on amorphous silica pools in
670   temperate soils, Biogeosciences, 8, 2281-2293, doi: 10.5194/bg-8-2281, 2011.

Conçalves, J.A., Henriques, R.: UAV photogrammetry for topographic monitoring of coastal areas, ISPRS Journal of
Photogrammetry and Remote Sensing, 104, 101-111, doi: 10.1016/j.isprsjprs.2015.02.009, 2015.

Cooke, J. and Leishman, M.R.: Tradeoffs between foliar silicon and carbon-based defences: evidence from vegetation
communities of contrasting soil types. Oikos, 121 (12), 2052-2060, doi: 10.1111/j.1600-0706.2012.20057.x, 2012.

675   Cornelis, J. T. and Delvaux, B.: Soil processes drive the biological silicon feedback loop, Funct. Ecol., 30, 1298–1310, doi:
10.1111/1365-2435.12704, 2016.

Cornelis, J. T., Ranger, J., Iserentant, A., and Delvaux, B.: Tree species impact the terrestrial cycle of silicon through various uptakes, Biogeochemistry, 97, 231-245, doi: 10.1007/s10533-009-9369-x, 2010.

Cui, Z. and Kerekes, J. P.: Potential of red edge spectral bands in future Landsat satellites on agroecosystem canopy green leaf area index retrieval, Remote Sens., 10, 1458, doi: 10.3390/rs10091458, 2018.

Dall'Asta, E., Roncella, R.A.: Comparison of Semiglobal and Local Dense Matching Algorithms for Surface Reconstruction, The International Archives of the Photogrammetry, Remote Sensing and Spatial Information Sciences, ISPRS Technical Commission V Symposium, XL-5, Riva del Garda, Italy, 23-25 June 2014, doi:10.5194/isprsarchives-XL-5-187-2014.

Desplanques, V., Cary, L., Mouret, J. C., Trolard, F., Bourrié, G., Grauby, O., and Meunier, J.-D.: Silicon transfers in a rice field in Camargue (France), Journal of Geochemical Exploration, 88, 190-193, doi: 10.1016/j.gexplo.2005.08.036, 2006.

Dunford, R., Michel, K., Gagnage, M., Piégay, H., and Trémelo, M.-L.: Potential and constraints of Unmanned Arial Vehicle technology for the characterization of Mediterranean riparian forest, Int. J. Remote Sens., 30:19, 4915-4935, doi: 10.1080/01431160903023025, 2009.

Dürr, H. H., Meybeck, M., Hartmann, J., Laruelle, G. G., and Roubeix, V.: Global spatial distribution of natural riverine silica inputs to the coastal zone, Biogeosciences, 8, 597-620, doi: 10.5194/bg-8-597, 2011.

Ehrlich, H., Demadis, K. D., Pokrovsky, O.S., and Koutsoukos, P. G.: Modern views on desilicification: biosilica and abiotic silica dissolution in natural and artificial environments, Chem. Rev., 110, 4656-4689, doi: 10.1021/cr900334y, 2010.

Elmer, M., Gerwin, W., Schaaf, W., Zaplata, M. K., Hohberg, K., Nenov, R., Bens, O., and Hüttl, R. F.: Dynamics of initial ecosystem development at the artificial catchment Chicken Creek, Lusatia, Germany, Environ. Earth Sci., 69, 491–505, doi: 10.1007/s12665-013-2330-2, 2013.

Epstein, E.: Silicon: its manifold roles in plants, Annals of Applied Biology, 155, 155-160, doi: 10.1111/j.1744-7348.2009.00343.x, 2009.

Fraysse, F., Pokrovsky, O. S., Schott, J., and Meunier, J. D.: Surface properties, solubility and dissolution kinetics of bamboo phytoliths, Geochimica et Cosmochimica Acta, 70, 1939-1951, doi: 10.1016/j.gca.2005.12.025, 2006.

Fraysse, F., Pokrovsky, O. S., Schott, J., and Meunier, J. D.: Surface chemistry and reactivity of plant phytoliths in aqueous solutions, Chemical Geology, 258, 197-206, doi: 10.1016/j.chemgeo.2008.10.003, 2009.

Frings, P. J., Clymans, W., Jeppesen, E., Lauridsen, T. L., Struyf, E., and Conley, D. J.: Lack of steady-state in the global biogeochemical Si cycle: emerging evidence from lake Si sequestration, Biogeochemistry, 117, 255-277, 2014.

Fuller, R. M., Groom, G. B., Mugisha, S., Ipulet, P., Pomeroy, D., Katende, A., Baily, R., and Ogutu-Ohwayo, R.: The integration of field survey and remote sensing for biodiversity assessment: a case study in the tropical forests and wetlands of Sango Bay, Uganda, Biological Conservation, 86, 379-391, doi: 10.1016/S0006-3207(98)00005-6, 1998.

Gamon, J. A., Field, C. B., Goulden, M. L., Griffin, K. L., Hartley, A. E., Joel, G., Penuelas, J., and Valentini, R.: Relationships between NDVI, Canopy Structure, and Photosynthesis in three Californian Vegetation Types, Ecological Applications, 5, 28-41, 1995.

710 Gerwin, W., Schaaf, W., Biemelt, D., Elmer, M., Maurer, T., and Schneider, A.: The Artificial catchment 'Hühnerwasser' (Chicken Creek): construction and initial properties, In: Hüttl, R.F., Schaaf, W., Biemelt, D., Gerwin, W. (Eds.), Ecosystem Development 1, pp. 58, 2010.

Gerwin, W., Schaaf, W., Biemelt, D., Winter, S., Fischer, A., Veste, M., and Hüttl, R. F.: Overview and first results of ecological monitoring at the artificial watershed Chicken Creek (Germany), Phys. Chem. Earth, 36, 61–73, doi: 715 10.1016/j.pce.2010.11.003, 2011.

Gonzáles, M. P., Bonaccorso, E., and Papeş, M.: Applications of geographic information systems and remote sensing techniques to conservation of amphibians in northwestern Ecuador, Global Ecology and Conservation, 3, 562-574, doi: 10.1016/j.gecco.2015.02.006, 2015.

Guntzer, F., Keller, C., Poulton, P. R., McGrath, S. P., and Meunier, J.-D.: Long-term removal of wheat straw decreases soil 720 amorphous silica at Broadbalk, Rothamsted, Plant and Soil, 352, 173-184, doi: 0.1007/s11104-011-0987-4, 2012.

Haboudane, D., Miller, J. R., Pattey, E., Zarco-Tejada, P. J., and Strachan, I. B.: Hyperspectral vegetation indices and novel algorithms for predicting green LAI of crop canopies: Modeling and validation in the context of precision agriculture, Remote Sens. Environ., 90, 337-352, doi: 10.1016/j.rse.2003.12.013, 2004.

Hodson, M. J., White, P. J., Mead, A., and Broadley, M. R.: Phylogenetic variation in the silicon composition of plants, Annals 725 of Botany, 96, 1027-1046, doi: 10.1093/aob/mci255, 2005.

Hugemann, W.: Correcting Lens Distortions in Digital Photographs; Ingenieurbüro Morawski +Hugemann: Leverkusen, Germany, 2010.

Husson, E., Hagner, O., and Ecke, F.: Unmanned aircraft systems help to map aquatic vegetation, Appl. Veg. Sci., 17, doi: 10.1111/avsc.12072, 567-577, 2014a.

730 Husson, E., Ecke, F., and Reese, H.: Comparison of manual mapping and automated object-based image analysis of non-submerged aquatic vegetation from very-high-resolution UAS images, Remote Sens., 8, 724, doi: 10.3390/rs8090724, 2016.

Kaczorek, D., Puppe, D., Busse, J., and Sommer, M.: Effects of phytolith distribution and characteristics on extractable silicon fractions in soils under different vegetation–An exploratory study on loess. Geoderma, 356, doi: 10.1016/j.geoderma.2019.113917, 2019.

735 Kaneko, K. and Nohara, S.: Review of effective vegetation mapping using the UAV (Unmanned Aerial Vehicle) Method, Journal of Geographic Information Systems, 6, 733-742, doi: 10.4236/jgis.2014.66060, 2014.

Katz, O., Puppe, D., Kaczorek, D., Prakash, N. B., Schaller, J.: Silicon in the soil–plant continuum: Intricate feedback mechanisms within ecosystems, Plants, 10, 4, 652, 2021.

Kavzoglu, T. and Mather, P. M.: The Use of Feature Selection Techniques in the Context of Artificial Neural Networks, 740 Proceedings of the 26th Annual Conference of the Remote Sensing Society, Leicester, UK, 12-14 September, unpaginated CD ROM, 2000.

Kelcey, J. and Lucieer, A.: Sensor Correction of a 6-Band Multispectral Imaging Sensor for UAV Remote Sensing, Remote Sens., 4, 1462-1493, doi: 10.3390/rs4051462, 2012.

Keller, C., Guntzer, F., Barboni, D., Labreuche, J., and Meunier, J. D.: Impact of agriculture on the Si biogeochemical cycle: input from phytolith studies, C. R. Geosci., 344, 739-746, doi: 10.1016/j.crte.2012.10.004, 2012.

Kodama, H. and Ross, G. J.: Tiron dissolution method used to remove and characterize inorganic components in soils, Soil Sci. Soc. Am. J., 55, 1180-1187, doi: 10.2136/sssaj1991.03615995005500040047x, 1991.

Kross, A., McNairn, H., Lapen, D., Sonohara, M., and Champagne, C.: Assessment of RapidEye vegetation indices for estimation of leaf area index and biomass in corn and soybean crops, Int. J. Appl. Earth Obs. Geoinf., 34, 235–248, doi: 10.1016/j.jag.2014.08.002, 2015.

Laliberte, A. S., Goforth, M. A., Steele, C. M., and Rango, A.: Multispectral Remote Sensing from Unmanned Aircraft: Image Processing Workflows and Applications for Rangeland Environments, Remote Sens., 3, 2529-2551, doi: 10.3390/rs3112529, 2011.

Lelong, C. C. D., Burger, P., Jubelin, G., Roux, B., Labbé, S., and Baret, F.: Assessment of Unmanned Aerial Vehicles Imagery for Quantitative Monitoring of Wheat Crop in Small Plots, Sensors, 8, 3557-3585, doi: 10.3390/s8053557, 2008.

Li, Z., Cornelis, J. T., Vander Linden, C., Van Ranst, E., Delvaux, B.: Neoformed aluminosilicate and phytogenic silica are competitive sinks in the silicon soil–plant cycle, Geoderma, 368, 114308, 2020.

Li, Z., Unzué-Belmonte, D., Cornelis, J.-T., Vander Linden, C., Struyf, E., Ronsse, F., Delvaux, B.: Effects of phytolithic rice-straw biochar, soil buffering capacity and pH on silicon bioavailability, Plant Soil, 438, 187-203, doi.org/10.1007/s11104-019-04013-0, 2019.

Li, Z., Delvaux, B.: Phytolith-rich biochar: A potential Si fertilizer in desilicated soils, GCB Bioenergy, 11, 1264-1282, doi: 10.1111/gcbb.12635, 2019.

Ma, J. F.: Role of silicon in enhancing the resistance of plants to biotic and abiotic stresses, Soil Science and Plant Nutrition, 50, 11-18, doi:10.1080/00380768.2004.10408447, 2004.

Ma, J. F. and Yamaji, N.: Silicon uptake and accumulation in higher plants, Trends in Plant Science, 11, 392-397, doi: 10.1016/j.tplants.2006.06.007, 2006.

Ma, J. F. and Takahashi, E.: Soil, fertilizer, and plant silicon research in Japan, Elsevier, Amsterdam, The Netherlands, 2002.

Madonsela, S., Azong Cho, M, Ramoelo, A., and Matunga, O.: Remote sensing of species diversity using Landsat 8 spectral variables, ISPRS J. Photogramm. Remote Sens., 133, 116-127, doi: 10.1016/j.isprsjprs.2017.10.008, 2017.

Mansouri, A., Marzani, F.S., Gouton, P.: Development of a protocol for CCD calibration: application to a multispectral imaging system, International Journal of Robotics and Automation, 3767, 1-12, DOI: 10.2316/Journal.206.2005.2.206-2784,2005.

Meng, B., Gao, J., Liang, T., Cui, X., Ge, J., Yin, J., Feng, Q., and Xie, H.: Modeling of alpine grassland cover based on Unmanned Arial Vehicle technology and multi-factor methods: A case study in the east of Tibetan Plateau, China, Remote Sens., 10, 320, doi: 10.3390/rs10020320, 2018.

Meunier, J. D., Guntzer, F., Kirman, S., and Keller, C.: Terrestrial plant-Si and environmental changes, Mineralogical Magazine, 72, 263-267, doi: 10.1180/minmag.2008.072.1.263, 2008.

Mundava, C., Helmholz, P., Schut, A. G. T., Corner. R., McAtee, B., and Lamb, D. W.: Evaluation of vegetation indices for rangeland biomass estimation in the Kimberly area of Western Australia, ISPRS Annals of the Photogrammetry, Remote Sensing and Spatial Information Sciences, ISPRS Technical Commission VII Symposium, Istanbul, Turkey, 29 September – 2 October 2014, Volume II-7.

Otukei, J. R. and Blaschke, T.: Land cover change assessment using decision trees, support vector machines and maximum likelihood classification algorithms, Int. J. Appl. Earth Obs. Geoinf., 12S, 27-31, doi: 10.1016/j.jag.2009.11.002, 2010.

Polis, G. A.: Why are parts of the world green? Multiple factors control productivity and the distribution of biomass, Oikos, 86, 3-15, 1999.

Pontigo, S., Ribera A., Gianfreda L., de la Luz Mora M., Nikolic M., and Cartes, P.: Silicon in vascular plants: uptake, transport and its influence on mineral stress under acidic conditions, Planta, 1-15, doi: 10.1007/s00425-015-2333-1, 2015.

Puppe, D., Kaczorek, D., Wanner, M., and Sommer, M.: Dynamics and drivers of the protozoic Si pool along a 10-year chronosequence of initial ecosystem states, Ecol. Eng., 70, 477-482, doi: 10.1016/j.ecoleng.2014.06.011, 2014.

Puppe, D., Ehrmann, O., Kaczorek, D., Wanner, M., and Sommer, M.: The protozoic Si pool in temperate forest ecosystems – Quantification, abiotic controls and interactions with earthworms, Geoderma, 243-244, 196-204, doi: 10.1016/j.geoderma.2014.12.018, 2015.

Puppe, D., Höhn, A., Kaczorek, D., Wanner, M., Sommer, M.: As Time Goes By – Spatiotemporal Changes of Biogenic Si Pools in Initial Soils of an Artificial Catchment in NE Germany, Appl. Soil Ecol., 105, 9-16, doi: 10.1016/j.apsoil.2016.01.020, 2016.

Puppe, D., Höhn, A., Kaczorek, D., Wanner, Wehrhan, M., and Sommer, M.: How big is the influence of biogenic silicon pools on short-term changes of water soluble silicon in soils? Implications from a study of a ten-year-old plant-soil-system, Biogeoscience, 14, 5239–5252, doi: 10.5194/bg-14-5239-2017, 2017.

Puppe, D. and Leue, M.: Physicochemical surface properties of different biogenic silicon structures: results from spectroscopic and microscopic analyses of protistic and phytogenic silica. Geoderma 330, 212-220, doi: 10.1016/j.geoderma.2018.06.001, 2018.

Puppe, D. and Sommer, M.: Experiments, uptake mechanisms, and functioning of silicon foliar fertilization – a review focusing on maize, rice, and wheat. Adv. Agron. 152, 1-49, doi: 10.1016/bs.agron.2018.07.003, 2018.

Puppe, D., Wanner, M., Sommer, M.: Data on euglyphid testate amoeba densities corresponding protozoic silicon pools, and selected soil parameters of initial and forested biogeosystems. Data in Brief 21, 1697-1703, doi: 10.1016/j.dib.2018.10.164, 2018.

Puppe, D., Kaczorek, D., Schaller, J., Barkusky, D., Sommer, M.: Crop straw recycling prevents anthropogenic desilication of agricultural soil–plant systems in the temperate zone–Results from a long-term field experiment in NE Germany, Geoderma, 403, 115187, 2021.

Puppe, D.: Review on protozoic silica and its role in silicon cycling. Geoderma 365, 114224, doi: 10.1016/j.geoderma.2020.114224, 2020.

Qi, J., Huete, A. R., Moran, M. S., Chehbouni, A., and Jackson, R. D.: Interpretation of vegetation indices derived from multi-temporal SPOT images, Remote Sens. Environ., 44, 89-101, doi: 10.1016/0034-4257(93)90105-7 1993.

Rebele, F. and Lehmann, C.: Biological flora of central Europe: *Calamagrostis epigejos* (L.) Roth, Flora, 196, 325-344, doi: 10.1016/S0367-2530(17)30069-5, 2001.

Rouse, J. W., Haas, R. H., Schell, J. A., and Deering, D.W.: Monitoring vegetation system in the great plains with ERTS, Proceedings of the Third Earth Resources Technology Satellite-1 Symposium, Greenbelt, USA, NASA SP-351, 3010-3017, 1974.

Sauer, D., Saccone, L., Conley, D. J., Herrmann, L., and Sommer, M.: Review of methodologies for extracting plant-available and amorphous Si from soils and aquatic sediments, Biogeochem., 80, 89-108, doi: 10.1007/s10533-005-5879-3, 2006.

Schaller, J., Roscher, C., Hillebrand, H., Weigelt, A., Oelmann, Y., Wilcke, W., Ebeling, A., and Weisser, W. W.: Plant diversity and functional groups affect Si and Ca pools in aboveground biomass of grassland systems, Oecologia, 182, 277-286, 2016.

Schaller, J., Hodson, M. J., and Struyf, E.: Is relative Si/Ca availability crucial to the performance of grassland ecosystems?, Ecosphere, 8, doi: 10.1002/ecs2.1726, 2017.

Schaller, J., Puppe, D., Kaczorek, D., Ellerbrock, R., Sommer, M.: Silicon cycling in soils revisited, Plants, 10, 2, 295, 2021.

Shafri, H. Z. M., Suhaili, A., and Mansor, S.: The Performance of Maximum Likelihood, Spectral Angle Mapper, Neural Network and Decision Tree Classifiers in Hyperspectral Image Analysis, J. Comput. Sci., 3, 419-423, doi: 10.3844/jcssp.2007.419.423, 2007.

Sommer, M., Kaczorek, D., Kuzyakov, Y., and Breuer, J.: Silicon pools and fluxes in soils and landscapes - a review, J. Plant Nutr. Soil Sci., 169, 310-329, doi: 10.1002/jpln.20052198, 2006.

Sommer, M., Jochheim, H., Höhn, A., Breuer, J., Zagorski, Z., Busse, J., Barkusky, D., Meier, K., Puppe, D., Wanner, M., and Kaczorek, D.: Si cycling in a forest biogeosystem - the importance of transient state biogenic Si pools, Biogeosciences, 10, 4991-5007, doi: 10.5194/bg-10-4991, 2013.

Song, Z., Müller, K., and Wang, H.: Biogeochemical silicon cycle and carbon sequestration in agricultural ecosystems, Earth-Science Reviews, 139, 268-278, doi: 10.1016/j.earscirev.2014.09.009, 2014.

Stoner, E. R. and Baumgardner, M. F.: Characteristic variations in reflectance of surface soils, Soil Sci. Soc. Am. J., 45, 1161-1165, 1981.

Strecha, C., Fletcher, A., Lechner, A., Erskine, P., and Fua, P.: Developing species specific vegetation maps using multi-spectral hyperspatial imagery from unmanned aerial vehicles, ISPRS Annals of the Photogrammetry, Remote Sensing and Spatial Information Sciences, XXII ISPRS Congress, Melbourne, Australia, 25 August – 01 September 2012, Volume I-3, 311-316 , 2012.

Struyf, E. and Conley, D. J.: Silica: an essential nutrient in wetland biogeochemistry, Frontiers in Ecology and the Environment, 7, 88-94, doi: 10.1890/070126, 2009.

845 Struyf, E. and Conley, D. J.: Emerging understanding of the ecosystem silica filter, Biogeochemistry, 107, 9-18, doi: 10.1007/s10533-011-9590-2, 2012.

Struyf, E., Smis, A., Van Damme, S., Garnier, J., Govers, G., Van Wesemael, B., Conley, D.J, Batelaan, O., Frot, E., Clymans, W., Vandevenne, F., Lancelot, C., Goos, P., and Meire, P.: Historical land use change has lowered terrestrial silica mobilization, Nature Communications, 1, 129, doi: 10.1038/ncomms1128, 2010.

850 Süß, K., Storm, C., Zehm, A., and Schwabe, A.: Succession in inland sand ecosystems: which factors determine the occurrence of the tall grass species *Calamagrostis epigejos* (L.) Roth and *Stipa capillata* L.?, Plant Biology, 6, 465-476, doi: 10.1055/s-2004-820871, 2004.

Thenkabail, P. S., Smith, R. B., and De Pauw, E.: Evaluation of Narrowband and Broadband Vegetation Indices for Determining Optimal Hyperspectral Wavebands for Agricultural Crop Characterization, Photogrammetric Engineering and 855 Remote Sensing, 68:6, 607-621, 2002.

Todd, S. W., Hoffer, R. M., and Milchunas, D. G.: Biomass estimation on grazed and ungrazed rangelands using spectral indices, Int. J. Remote Sens., 19:3, 427-438, doi: 10.1080/014311698216071, 1998.

Tréguer, P. J. and De La Rocha, C. L.: The world ocean silica cycle, Ann. Rev. Mar. Sci., 5, 477-501, doi: 10.1146/annurev-marine-121211-172346, 2013.

860 Tréguer, P. and Pondaven, P.: Global change: silica control of carbon dioxide, Nature, 406, 358-359, doi: 10.1038/35019236, 2000.

Tucker, J. J.: Red and photographic infrared linear combinations for monitoring vegetation, Remote Sens. Environ., 8, 127-150, 1979.

Turner, D., Lucieer, A., Malenovský, Z., King, D. H., and Robinson, S.A.: Spatial Co-Registration of Ultra-High Resolution 865 Visible, Multispectral and Thermal Images Acquired with a Micro-UAV over Antarctic Moss Beds, Remote Sens. 6, 4003-4024, doi: 10.3390/rs6054003, 2014.

Vandevenne, F., Struyf, E., Clymans, W., and Meire, P.: Agricultural silica harvest: have humans created a new loop in the global silica cycle?, Frontiers in Ecology and the Environment, 10, 243-248, doi: 10.1890/110046, 2012.

Vandevenne, F. I., Barão, L., Ronchi, B., Govers, G., Meire, P., Kelly, E. F., and Struyf, E.: Silicon pools in human impacted 870 soils of temperate zones, Global Biogeochemical Cycles, 29, 1439-1450, doi: 10.1002/2014GB005049, 2015a.

Vandevenne, F. I., Delvaux C., Hughes H. J., André L., Ronchi B., Clymans W., Barão L., Govers G., Meire, P., and Struyf, E.: Landscape cultivation alters δ^{30}Si signature in terrestrial ecosystems, Scientific Reports, 5, 7732, doi: 10.1038/srep07732, 2015b.

VDLUFA: Methodenbuch Band I: Die Untersuchung von Böden, Kapitel 6.2.1.2., VDLUFA Verlag, Speyer, 1991.

875 Wang, J., Rich, P. M., Price, K. P., and Kettle, W. D.: Relationship between NDVI, Grassland Production, and Crop Yield in the Central Great Plains, Geocarto International, 20, 5-11, doi: 10.1080/10106040508542350, 2005.

Wehrhan, M., Rauneker, P., and Sommer, M.: UAV-based Estimation of Carbon Exports from Heterogeneous Soil Landscapes – A Case Study from the CarboZALF Experimental Area, Sensors, 16, 255, doi: 10.3390/s16020255, 2016.

Xu, N., Tian, J., Tian, Q., Xu, K., and Tang, S.: Analysis of vegetation red edge with different illuminated/shaded canopy proportions and to construct Normalized Difference Canopy Shadow Index, Remote Sens., 11, 1192, doi:10.3390/rs11101192, 2019.

Yang, X., Zhaoliang, S., Chang, Y., Fan, D.: Quantification of different silicon fractions in broadleaf and conifer forests of northern China and consequent implications for biogeochemical Si cycling, Geoderma, 361, 114036, doi.org/10.1016/j.geoderma.2019.114036, 2020.

Yang, X., Zhaoliang, S., Zhilian, Q., Wu, L., Yin, L., Van Zwieten, L., Song, A., Ran, X., Yu, C., Wang, H.: Phytolith-rich straw application and groundwater table management over 36 years affect the soil-plant silicon cycle of a paddy field, Plant Soil, 454, 343-358, doi.org/10.1007/s11104-020-04656-4, 2020.

Zaplata, M. K., Winter, S., Biemelt, D., and Fischer, A.: Immediate shift towards source dynamics: the pioneer species Conyza canadensis in an initial ecosystem, Flora, 206, 928-934, doi: 10.1016/j.flora.2011.07.001, 2011a.

Zaplata, M. K., Fischer, A., and Winter, S.: Vegetation patterning. In: Elmer, M., Schaaf, W., Biemelt, D., Gerwin, W., Hüttl, R.F. (eds.). The artificial catchment 'Chicken Creek' – initial ecosystem development 2005-2010, Ecosystem Development, 3, BTU Cottbus, pp. 67-92, 2011b.

Zaplata, M. K., Winter, S., Fischer, A., Kollmann, J., and Ulrich, W.: Species-driven phases and increasing structure in early-successional plant communities, The American Naturalist, 181, E17-E27, doi: 10.1086/668571, 2013.

Zarco-Tejada, P. J., Hornero, A., Hernandez-Clemente, R., and Beck, P.S.A.: Understanding the temporal dimension of the red –edge spectral region for forest decline detection using high-resolution hyperspectral and Sentinel-2a imagery, ISPRS J. Photogramm. Remote Sens., 137, 134-148, doi: 10.1016/j.isprsjprs.2018.01.017, 2018.

Zweig, C. L., Burgess, M. A., Percival, H. F., and Kitchens, W. M.: Use of unmanned aircraft systems to delineate fine-scale wetland vegetation communities, Wetlands, 35, 303–309, doi: 10.1007/s13157-014-0612-4, 2015.